INTERNATIONAL JOURNAL FOR NUMERICAL METHODS IN BIOMEDICAL ENGINEERING
Int. J. Numer. Meth. Biomed. Engng. 0000; **00**:1–31
Published online in Wiley InterScience (www.interscience.wiley.com). DOI: 10.1002/cnm

Extended Finite Element Method for Fluid-Structure Interaction in Wave Membrane Blood Pump

Marco Martinolli [1] , Jacopo Biasetti [2] *, Stefano Zonca [1] , Luc Polverelli [2] , Christian Vergara [3] †

[1]*MOX, Dipartimento di Matematica, Politecnico di Milano, Milan, Italy*
[2]*CorWave SA, Clichy, France*
[3]*LaBS, Dipartimento di Chimica, Materiali e Ingegneria Chimica "Giulio Natta", Politecnico di Milano, Milan, Italy*

SUMMARY

Numerical simulations of cardiac blood pump systems are integral to the optimization of device design, hydraulic performance and hemocompatibility. In wave membrane blood pumps, blood propulsion arises from the wave propagation along an oscillating immersed membrane, which generates small pockets of fluid that are pushed towards the outlet against an adverse pressure gradient. We studied the Fluid-Structure Interaction between the oscillating membrane and the blood flow via three-dimensional simulations using the Extended Finite Element Method, an unfitted numerical technique that avoids remeshing by using a fluid fixed mesh. Our three-dimensional numerical simulations in a realistic pump geometry highlighted, for the first time in this field of application, that XFEM is a reliable strategy to handle complex industrial problems. Moreover, they showed the role of the membrane deformation in promoting a blood flow towards the outlet despite an adverse pressure gradient. We also simulated the pump system at different pressure conditions and we validated the numerical results against *in-vitro* experimental data. Copyright © 0000 John Wiley & Sons, Ltd.

Received . . .

KEY WORDS: Fluid-Structure Interaction, Wave membrane blood pump, Extended Finite Element Method, Model validation

CONTENTS

†Correspondence to: *Christian Vergara, Piazza Leonardo da Vinci 32, 20133, Milan, Italy. christian.vergara@polimi.it
*Currently working at AstraZeneca R&D AB, Mölndal, Sweden

Prepared using cnmauth.cls *[Version: 2010/03/27 v2.00]*

1. INTRODUCTION

Heart failure is a global pandemic disease that affects more than 60 million people worldwide, a number which will continue to increase in the next decades [1, 2]. To address this challenge, there is an increasing interest in developing reliable *mechanical circulatory support* devices which take over, totally or partially, the pumping function of the failing heart. These devices can be employed as bridge to heart transplantation or as destination therapy, to permanently support heart function.

Ventricular Assist Devices (VADs) [3, 4], which are designed to support the heart's ventricle function, are becoming the standard of care for patients with end-stage heart failure. In comparison to other devices (such as *total artificial hearts* [5]), VADs have proved to be less invasive, featuring better performance in terms of hemocompatibility and risk of adverse events [4].

In *Left-Ventricular Assist Devices* (LVADs), blood pumps collect the blood from the left ventricular chamber and eject it into the ascending aorta via a flexible cannula. The standard blood pumps currently available for clinical use are rotary pumps, based on the rotation of an internal impeller that imparts kinetic energy to the blood. Rotary pumps are divided in axial [6, 7] and centrifugal flow pumps [8, 9, 10], depending on the direction of the imparted blood acceleration [3]. However, rotary pumps cause damage to blood elements producing hemolysis, thrombosis, and bleeding complications because of the elevated velocity gradients of their rotors [11, 12]. Furthermore, since these pumps are operated at a single pump speed, their clinical use results in a reduction of patient pulse pressure and, consequently, to possible complications related to continuous non-physiologic blood pumping, such as gastro-intestinal bleeding, aortic valve insufficiency or stroke [4]. Therefore, LVAD companies have developed pulsation algorithms for rotary pumps, with the aim of improving wash-out in the pumps and reducing thrombosis. However, the LVAD pulsation algorithms currently used clinically do not restore a physiologic pulse [13].

Prepared using cnmauth.cls
DOI: 10.1002/cnm

With the aim to overcome the drawbacks of rotary pumps, CorWave SA (Clichy, France) is developing a novel LVAD, referred to as *wave membrane blood pump* or *progressive wave blood pump*, which employs an innovative pumping technology based on the gentle propelling action of an undulating elastic membrane on the blood. Compared with current rotary VADs, wave membrane blood pumps have two major advantages: i) the membrane generates smaller shear stresses and may provoke less trauma on the blood cells; ii) due to the low inertia of the membrane, the oscillation frequency can be rapidly changed to alter hydraulic performance in order to get physiologic flow, potentially reducing the risks of complications like stroke, non-surgical bleeding and renal dysfunction. This novel fluid propulsion approach requires a deep insight into the fluid-structure dynamics arising within the pump.

Mathematical modeling and numerical simulations are valuable tools in the field of cardiovascular medicine, allowing to better understand the complex processes involved in cardiovascular diseases and to support clinical decisions in treatments and surgical procedures [14, 15, 16, 17]. Particularly, in the case of biomedical devices, computational simulations are widely used to investigate and optimize performance under different clinical conditions. Among others, we mention the following fields of application: the optimization of coronary arterial bypass grafts to reduce critical factors, like flow vorticity and wall shear stress rate [18, 19]; the study of blood dynamics in *transcatheter aortic valve*, a biological prosthesis that replaces the native aortic valve in patients with high-risk valve diseases [20, 21, 22, 23]; the performance of *drug-eluting stents*, which prevent restenosis by local releasing of a specific drug [24, 25, 26, 27]; the study of optimal anastomotic angle in arteriovenous fistula for hemodialysis [28, 29].

In the case of VADs, Computational Fluid Dynamics (CFD) has proven to be a powerful tool to improve the pump performance and efficiency, while reducing blood trauma. Indeed, starting in the 1990s with the first numerical studies carried out in simplified pump models [30, 31], *in silico* simulations emerged to be more time- and cost-effective than *in vitro* or *in vivo* testings, overcoming limitations in prototype fabrication and experimental setup [12]. In the last decades, there have been plenty of numerical studies concerning the design and performance of rotary blood pumps. Among these, we mention, for instance: parametric studies of geometric features in centrifugal [32, 33] and axial pumps [34], to analyze the effects on hydraulic efficiency and stagnation time; CFD-based optimization of the pump design to avoid retrograde leakage flow [35, 36]; computational study of the effect of the impeller position in a magnetically levitated blood pump [37]. Other works focused on the optimal implantation of the device [38, 39, 40, 41] or on the hemocompatibility requirements of VADs, trying to understand and prevent the mechanisms that favor hemolysis [42, 43, 44], thrombogenicity [45, 46, 47], and gastrointestinal bleeding [48].

Regarding progressive wave blood pumps, to our knowledge the only reference is the work from Perschall et al. [49], who performed a Fluid-Structure Interaction (FSI) study, providing a validation of their results against experimental data. FSI numerical experiments have been carried out by considering a 2D axi-symmetric approximation of the discoidal geometry and the Arbitrary

Prepared using cnmauth.cls
DOI: 10.1002/cnm

Lagrangian-Eulerian (ALE) formulation. Moreover, a Design Of Experiment (DOE) method is applied to build a virtual prototype of the tubular design by the accurate tuning of geometric parameters, like membrane diameter, membrane thickness or pump walls angle.

The objective of this paper is to provide a significant step forward with respect to [49], by means of numerical investigation of the pump functioning in a three-dimensional realistic pump domain for different key functional parameters. To this aim, we need to identify a numerical strategy that is able to accurately describe the behaviour of a thin wave membrane immersed in the blood flow, which undergoes relatively large displacements with regard to the surrounding narrow fluid region. Indeed, the membrane may oscillate enough to approach closely to the boundaries of the fluid domain reaching a *quasi-contact* configuration with the pump walls. In this context, fitted methods like ALE-based techniques [50, 51, 52] and Space-Time Finite Elements [53, 54, 55, 56, 57] could be used. However, due to excessive distortion of the fluid mesh due to the quasi-contact, they would require frequent remeshing procedures. Alternatively, unfitted methods may be considered. These techniques are specifically designed to avoid remeshing issues by using a fixed background mesh for the fluid and an overlapping solid mesh which is free to move on the foreground, leading to split fluid mesh elements. The most important unfitted techniques are: Immersed Boundary (IB) [58, 59, 60], Fictitious Domain (FD) [61, 62, 63], Extended Finite Element Method (XFEM) [64, 65, 66, 67], and polygonal Discontinuous Galerkin (PolyDG) method [68].

In the framework of XFEM, the degrees of freedom (d.o.f.) of the split elements are doubled so that the solution can be integrated independently in the two split sub-regions, thus permitting an internal discontinuity [69, 70, 71]. XFEM is capable of capturing the fluid-structure interface without loss of accuracy and has already proven to be an effective, robust and versatile numerical strategy to solve FSI problems with thin immersed membranes, both in 2D [72, 64, 67] and in 3D [73, 74]. However, at the best of our knowledge, nowadays it has been mostly applied to academic problems, while we are not aware of any example of 3D industrial application. Due to its accuracy and versatility in managing FSI problems with complex immersed structure dynamics, we believe that it could be an effective tool for the solution of problem in real and complex geometries. For this reason, in this work we adopted an XFEM-based strategy to handle the FSI problem arising in our progressive wave blood pump, showing that this method is in fact suitable also for industrial problems.

The structure of this paper is the following: in Section 2, we describe the working mechanisms of the wave membrane blood pump under study; in Section 3, we introduce the mathematical formulation of the FSI model together with its numerical discretization; in Section 4, we present the results of the numerical simulations for different pressure conditions and we validate the model against experimental data; in Section 5, we draw the main conclusions of the current study.

Prepared using cnmauth.cls
DOI: 10.1002/cnm

2. PUMP FUNCTIONING PRINCIPLE

In case of heart failure, the cardiac function is compromised and only a reduced volume of oxygenated blood is ejected into circulation, leading to poor oxygenation of the tissues. Therefore, blood pumps are implanted at the apex of the failing heart to collect part of the blood from the left ventricle in the pump chamber and mechanically pump it into the distal aorta via a flexible outlet cannula (Figure 1, left). In particular, progressive wave pumps differ from other LVADs for utilizing an innovative pumping mechanism based on the mutual interaction between an elastic undulating membrane and the blood flow, with the potential to produce physiologic flow rates with minimum blood trauma.

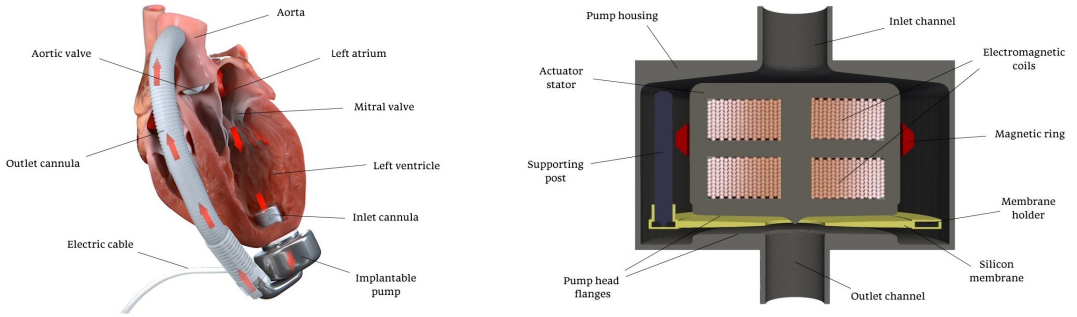

Figure 1. Left: Blood path through the left heart with an implanted LVAD. The oxygenated blood coming from the left atrium is collected into the implantable pump apparatus placed at the left ventricle apex, and then ejected into the proximal aorta via an outlet cannula. Right: Cross sectional view of the main components of the implantable wave membrane pump, including inlet and outlet channel, the actuator assembly (stator, electromagnetic coils and magnet ring), the membrane assembly (silicon membrane and membrane holder), and one (of the three) supporting posts. The diameter of the device is 5 cm long, while its overall height is of about 4 cm.

The main components of the membrane wave pump are shown in the right panel of Figure 1 and correspond to the inlet and the outlet cannula, the actuator assembly and the membrane assembly. The inlet and the outlet channels are located at the opposite ends of the pump cylindrical body. The actuator assembly is composed of a stationary part, consisting of the central stator and the electromagnetic coils, and a mobile part, the *magnet ring*, that is suspended concentrically around the stator. The membrane assembly consists of the silicon membrane and the membrane holder. The silicon membrane is a discoidal polymer elastic body that is displaced concentrically to the pump axis, in the pump head region, i.e. a narrow space proximal to the outlet channel delimited by rigid walls of the pump housing, called *pump head flanges*. Both the gap between these flanges and the membrane thickness gradually decrease going towards the inner circular opening. The membrane holder is a rigid titanium ring that is enclosed in the most external part of the membrane disc and that is connected to the magnet ring by means of three supporting posts placed equidistantly over the actuator circumference.

The action of the blood pump is driven by the electromagnetic actuator which triggers the undulating motion of the flexible silicon membrane. An alternating current is applied to the coils to

Prepared using cnmauth.cls
DOI: 10.1002/cnm

generate a magnetic field that guides the periodic displacement of the magnet ring and, consequently, of the membrane holder. Notice that the motion of the magnet ring is axially constrained because of the presence of suspension rings which do not permit radial displacements. In this way, the actuator exerts a periodic excitation force that is substantially normal to the membrane disc, inducing a wavelike displacement which propagates in the membrane medium from the membrane holder towards the center in direction of the outlet channel. Therefore, this progressive wave propagation along the membrane transports the blood that is enclosed in the spaces between the membrane wave and the pump head flanges radially inward towards the outlet channel. These masses of blood transported by the membrane wave are referred to as *fluid pockets*. During its wave motion, the membrane may approach to the pump flanges very closely, resulting in a *quasi-contact* configuration that allows to isolate the fluid pockets and to minimize any potential backflow from the outlet towards the inlet, thus increasing the pump efficiency. Moreover, the membrane displacement gets damped by the effect of the surrounding viscous fluid, provoking an energy transfer to the blood that ends up in the form of pressure buildup and addition of kinetic energy. The characteristics of the pressure gradient and the blood flow depend on the size and the shape of the membrane, the spacing between the pump head flanges, and the excitation parameters. Thus, the pump works as an energy transducer, that converts electromechanical energy into hydraulic power.

This pump system has the potential to generate a wide range of physiological flow rates and, in particular, to mimic the pulsatility induced by the native heart. Indeed, in principle, we could vary the operating parameters of the pump during the cardiac cycle: during systole the pump outflow rate could be increased to reproduce the natural augmentation of the cardiac output, while during diastole the operating point of the pump can be decreased to avoid backflow and left ventricle regurgitation. However, in this work we study the pump system at fixed operating conditions, as done in experimental tests forpump hydraulic characterization. Notice that, given the oscillatory nature of the wave membrane technology, the outflow signal results to be pulsatile in time even at fixed operating conditions.

The pump model of our study is similar to the discoidal design described in Perschall et al. [49], but there are important differences: (i) in the prototype in Perschall's work we find two inlet channels located 180 degrees apart, while in our case we have a unique inlet, that results in a more homogeneous flow field; (ii) our pump actuator is magnetic, not mechanic, so that we avoid the need of contact seals or bearings.

The pump device is coupled with an external controller, that sets the oscillation frequency and voltage applied to the coils in the actuator, and a set of extracorporeal batteries, to power the system. An external programmer is used to configure the working parameters of the pump. .

DOI: 10.1002/cnm

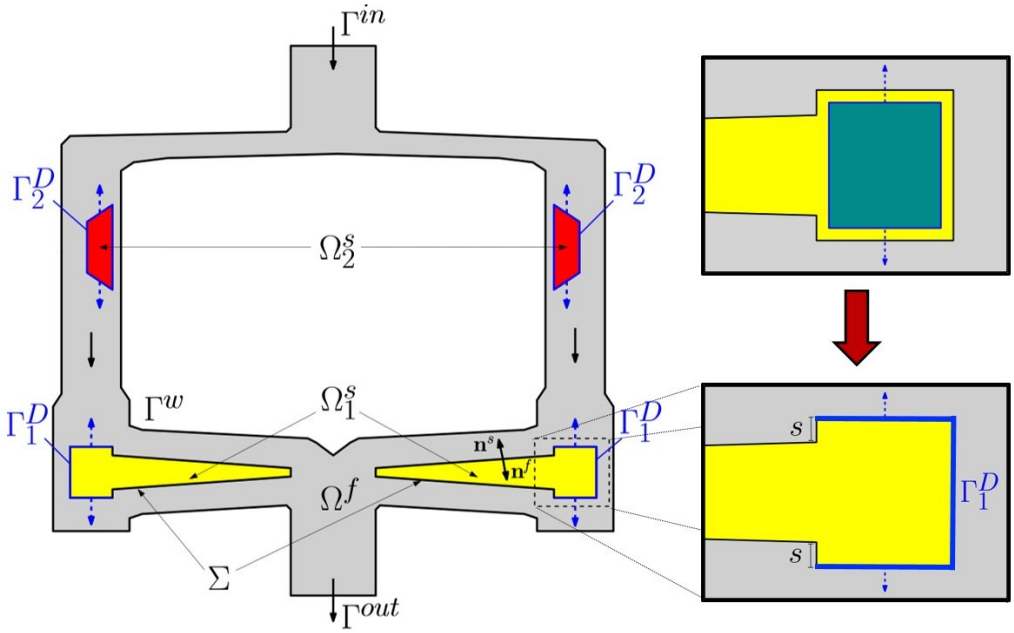

Figure 2. Cross-sectional representation of the mathematical domain of interest, consisting of the fluid domain Ω^f (grey), the membrane assembly Ω_1^s (yellow) and the magnet ring Ω_2^s (red). Γ^{in} and Γ^{out} indicate the inlet and the outlet boundary, respectively; while Γ^w refers to the wall boundary. Γ_1^D and Γ_2^D (blue) indicate the surface of the membrane frame and the magnet ring, respectively, where a Dirichlet condition is applied; the boundary Σ is the free fluid-structure interface.

3. MATHEMATICAL AND NUMERICAL METHODS

3.1. Mathematical model

In this section, we describe the mathematical approach employed to model the interaction between the blood and the oscillating structure in the progressive wave blood pump.

Let Ω be the whole pump domain composed by the region occupied by the fluid and by the immersed oscillating structures. The latter are composed by three main components:

- The *membrane assembly* $\Omega_1^s(t)$ (yellow region in Figures 1, right, and 2, left). It is composed by a flexible region, referred to as the *flexible membrane*, and a rigid region, referred to as the *membrane frame* (see zoom in Figure 2, right). The first region interacts with the fluid through the fluid-structure interface $\Sigma(t)$, where the wave displacement propagates towards the inner orifice of the membrane disc; here no-slip and traction continuity conditions hold true. The second region interacts with the fluid through the interface $\Gamma_1^D(t)$. However, here the motion is not determined by the interaction with the fluid, rather by the movement of the membrane holder (green sub-component in Figure 2, right). For the sake of simplicity, we assume that the movement of the region delimited by Γ_1^D is completely rigid, so that we can apply a displacement field $\boldsymbol{\varphi}$ directly on Γ_1^D as a Dirichlet condition, see right panel in Figure 2. Accordingly, for the fluid we prescribed a compatible Dirichlet data $\dot{\boldsymbol{\varphi}}$ on Γ_1^D. Notice that,

Prepared using cnmauth.cls
DOI: 10.1002/cnm

since we are prescribing two Dirichlet conditions with known data, we cannot say anything about the interface tractions.

- The magnet ring $\Omega_2^s(t)$ (red region in Figures 1, right, and 2). Like the membrane holder, its movement is determined by the pump actuator and thus compatible Dirichlet conditions have been again prescribed at the interface $\Gamma_2^D(t)$ (see Figure 2) both for fluid and structure. Notice that, since the magnet ring is mechanically joined to the membrane holder, the whole complex moves rigidly and therefore the same data φ and $\dot{\varphi}$ have been prescribed on the magnet ring.

- The supporting posts (dark blue region in Figure 1). Unlike the magnet ring that surrounds the actuator and thus occupies all the fluid path region, these posts are three thin columns whose presence should not influence significantly blood flow dynamics. For this reason, we decided here to neglect the posts in our domain. In any case, specific investigations on their real influence will be the subject of future studies.

Then, the fluid domain $\Omega^f(t)$ is determined by

$$\Omega^f(t) = \Omega \setminus \Omega^s(t), \tag{1}$$

with $\Omega^s(t) = \Omega_1^s(t) \cup \Omega_2^s(t)$.

The intertwined dynamics arising inside a wave membrane pumps can be mathematically described in the framework of FSI modeling, where a system of partial differential equations describes separately the behaviour of the fluid and of the structure in the respective domains, while proper coupling conditions define their interaction at the interface Σ.

In particular, we assumed the blood to be an incompressible, viscous and Newtonian fluid, because, apart from local (in space and time) exceptions in the *quasi-contact* region, the characteristic size of the pump domain is generally much larger than the diameter of blood cells. Denoting by ρ^f the fluid density and by μ^f the dynamic viscosity, we can then express the fluid Cauchy stress tensor as $\mathbf{T}^f(\mathbf{u}, p) = -p\mathbf{I} + 2\mu^f \mathbf{D}(\mathbf{u})$, with $\mathbf{D}(\mathbf{u}) = \frac{1}{2}(\nabla\mathbf{u} + \nabla\mathbf{u}^T)$, where $\mathbf{u}$ and p are the fluid velocity and pressure, respectively. Therefore, we used the Navier-Stokes equations to model the conservation of momentum and mass of blood, respectively.

Concerning the structural problem, the membrane disc domain Ω_1^s and the magnet ring domain Ω_2^s are both considered to be elastic bodies made of homogeneous and isotropic material, as reported in [49], but feature different material properties. Therefore, to shorten the formulation we have written the structural problem for the whole domain Ω^s with density spatial function $\widetilde{\rho}^s(\mathbf{x}) = \rho_1^s$ if $\mathbf{x} \in \Omega_1^s$ and $\widetilde{\rho}^s(\mathbf{x}) = \rho_2^s$ if $\mathbf{x} \in \Omega_2^s$. Analogous definitions were used for Lamé parameters $\widetilde{\lambda}_s(\mathbf{x})$ and $\widetilde{\mu}^s(\mathbf{x})$. We also assumed that the structures undergo infinitesimal linear deformations, so that we can apply Hooke's Law in the range of small displacements and write the first Piola-Kirchhoff tensor as $\widehat{\mathbf{T}}^s(\widehat{\mathbf{d}}) = \widetilde{\lambda}^s\,(\widehat{\nabla}\cdot\widehat{\mathbf{d}})\,\mathbf{I} + 2\widetilde{\mu}^s\,\widehat{\mathbf{D}}(\widehat{\mathbf{d}})$, where $\widehat{\mathbf{d}}$ is the structure displacement. Notice that we use superscript $\widehat{\cdot}$ to refer to quantities defined in the Lagrangian configuration in the domain $\widehat{\Omega}^s = \Omega^s(0)$. We remark that the small displacement approximation is justified in our problem

Prepared using cnmauth.cls
DOI: 10.1002/cnm

setting, because the observed normal strains are smaller than 5.5% and the tangential shears are smaller than 3%.

For a given $T > 0$, the fluid-structure interaction problem reads as follows: for each time $t \in (0, T]$, find the fluid velocity $\mathbf{u}(t) : \Omega^f(t) \to \mathbb{R}^3$, the fluid pressure $p(t) : \Omega^f(t) \to \mathbb{R}$, and the structure displacement $\widehat{\mathbf{d}}(t) : \widehat{\Omega}^s \to \mathbb{R}^3$, such that:

$$\rho_f \left(\partial_t \mathbf{u} + \mathbf{u} \cdot \nabla \mathbf{u}\right) - \nabla \cdot \mathbf{T}^f(\mathbf{u}, p) = \mathbf{0} \qquad \text{in } \Omega^f(\mathbf{d}), \tag{2a}$$

$$\nabla \cdot \mathbf{u} = 0 \qquad \text{in } \Omega^f(\mathbf{d}), \tag{2b}$$

$$\widetilde{\rho}_s \partial_{tt} \widehat{\mathbf{d}} - \widehat{\nabla} \cdot \widehat{\mathbf{T}}^s(\widehat{\mathbf{d}}) = \mathbf{0} \qquad \text{in } \widehat{\Omega}^s, \tag{2c}$$

$$\mathbf{u} = \partial_t \mathbf{d} \qquad \text{on } \Sigma(\mathbf{d}), \tag{2d}$$

$$\mathbf{T}^f(\mathbf{u}, p)\, \mathbf{n}^f = -\mathbf{T}^s(\mathbf{d})\, \mathbf{n}^s \qquad \text{on } \Sigma(\mathbf{d}), \tag{2e}$$

where $\mathbf{T}^s$ in Equation (2e) is the solid Cauchy stress tensor, that is the Eulerian counterpart of the first Piola-Kirchhoff tensor, defined as $\mathbf{T}^s(\mathbf{d}) = J^{-1}\, \widehat{\mathbf{T}}^s(\widehat{\mathbf{d}})\, \mathbf{F}^T$, with $\mathbf{F} = \nabla \mathbf{x}$ being the gradient of deformation and $J = \det \mathbf{F}$ its determinant. We remark that in the small displacement regime we could assume that $\widehat{\mathbf{T}}^s = \mathbf{T}^s$. In the system (2), we have highlighted the dependence of the fluid domain Ω^f (and thus of the interface Σ) on the structure displacement $\mathbf{d}$ through its definition (1) (*geometric coupling*).

In System (2), Equations (2a) and (2b) are the non-linear incompressible Navier-Stokes equations, while Equation (2c) is the linearized elastodynamic equations. Equations (2d) and (2e) are the coupling conditions imposed on the interface Σ guaranteeing the continuity of velocity and of tractions, respectively, and where $\mathbf{n} = \mathbf{n}^f = -\mathbf{n}^s$ is the external fluid normal. We highlight that the combination of the incompressibility of the fluid (Equation (2b)) with the no-slip kinematic condition (2d) allows to consider a *quasi-contact* assumption when the membrane and the pump walls come into contact. Indeed, previous studies [75, 76] showed that in such conditions, from the mathematical and numerical point of view, contact - strictly speaking - cannot occur when a moving body approaches to a wall, because the interstitial fluid cannot slip away and allow for actual collision. Therefore, despite physical contact may occur between the membrane and the pump head flanges under certain operating conditions of the pump, no contact models were introduced.

Referring to Figure 2, system of equations (2) has to be closed with proper initial and boundary conditions. For the fluid problem, we considered Neumann conditions both at the inlet Γ^{in} and at the outlet Γ^{out} to represent the pressure difference of the pump. We also applied an homogeneous Dirichlet condition at the pump walls Γ^w. Finally, in order to model the effect of the actuator on the motion of the membrane frame and the magnet ring, as anticipated we impose Dirichlet conditions

Prepared using cnmauth.cls
DOI: 10.1002/cnm

on $\Gamma^D = \Gamma_1^D \cup \Gamma_2^D$. In summary, we have:

$$\mathbf{T}^f(\mathbf{u}, p)\,\mathbf{n}^f = \left(P^{out} - \Delta P\right)\,\mathbf{n}^f \qquad \text{on } \Gamma^{in}, \tag{3a}$$

$$\mathbf{T}^f(\mathbf{u}, p)\,\mathbf{n}^f = P^{out}\,\mathbf{n}^f \qquad \text{on } \Gamma^{out}, \tag{3b}$$

$$\mathbf{u} = \mathbf{0} \qquad \text{on } \Gamma^{w}, \tag{3c}$$

$$\mathbf{d} = \boldsymbol{\varphi} \qquad \text{on } \Gamma^{D}, \tag{3d}$$

$$\mathbf{u} = \dot{\boldsymbol{\varphi}} \qquad \text{on } \Gamma^{D}, \tag{3e}$$

where P^{out} is a given outlet pressure value and $\Delta P > 0$ is the pump head pressure, corresponding to the pressure difference between the pump outlet and the inlet. At time $t = 0$, we finally imposed the initial conditions $\mathbf{u}(0) = \mathbf{u}_0$, $\mathbf{d}(0) = \mathbf{d}_0$ and $\dot{\mathbf{d}}(0) = \mathbf{w}_0$. In our application, we considered null initial conditions, i.e. $\mathbf{u}_0 = \mathbf{0}$, $\mathbf{d}_0 = \mathbf{0}$ and $\mathbf{w}_0 = \mathbf{0}$.

3.2. Numerical methods

3.2.1. The Extended Finite Element Method Numerical methods for FSI problems are divided into fitted and unfitted methods, depending whether the fluid and solid meshes are fitted to each other or not. In case of fitted methods, the meshes move together. Although they present undoubted good properties like the easiness of implementation, for our problem we decided to consider an unfitted method for the following reasons: i) they prevent high distortion of the fluid elements due to the wave motion of the membrane in the limited pump head region (see Section 2) and thus frequent remeshing; ii) the *quasi-contact* assumption between the membrane and the pump walls is relatively easily to implement efficiently. Notice that remeshing does not only represent an extra burden on the computational time of the simulation, but it may also affect the quality of the solution, depending on the accepted tolerance on the mesh quality index (*e.g.*, aspect ratio of the elements). Indeed, in similar applications we observed that, if this tolerance is too large, we can have convergence issues due to severe distortions of fluid elements; while, if it is too small, the interpolation inherent in the remeshing process can introduce errors in the fluid solution.

Among the unfitted methods, we selected the Extended Finite Element Method (XFEM), proposed in [71], which is based on the extension of the features of the classical Finite Elements and allows to have higher geometrical flexibility without loss of accuracy. Thanks to such extension, solutions with discontinuities are well described and complex problems with immersed interfaces or structures could be accurately solved. XFEM has proven to be an effective strategy for many problems, in particular for FSI with immersed structures [64, 77, 65, 67], maintaining a good accuracy at the fluid-structure interface. For our study, we specifically refered to the 3D formulation reported in [73], which treats the case of a 3D thin structure, by using a Discontinuous Galerkin (DG) mortaring to weakly impose the continuity conditions (2d)-(2e) at the interface.

Prepared using cnmauth.cls
DOI: 10.1002/cnm

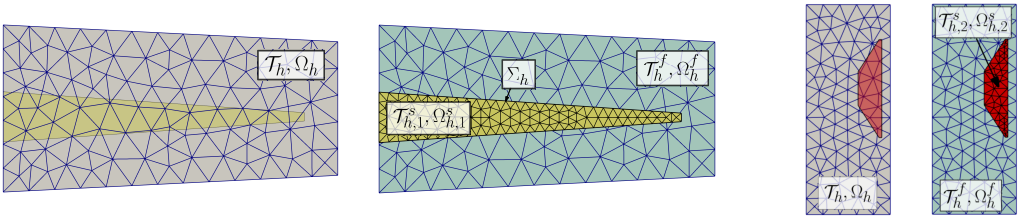

Figure 3. Global mesh $\mathcal{T}_h$ (gray) is overlapped by the structure meshes $\mathcal{T}_{h,1}^s$ (membrane assembly, in yellow) and $\mathcal{T}_{h,2}^s$ (magnet ring, in red). Fluid cut mesh $\mathcal{T}_h^f$ in light blue.

Let $\Omega_h^{f,n} \simeq \Omega^f(t^n)$ and $\Omega_h^{s,n} \simeq \Omega^s(t^n)$ be the approximated fluid and structure domains after space (XFEM) and time discretization, the latter being based on the timestep parameter $\Delta t > 0$ such that $t^n = n\Delta t$ for $n = 1, 2, \ldots$.

In the framework of XFEM, a global mesh $\mathcal{T}_h$ defined in Ω_h is kept fixed on the background, while a structure mesh $\mathcal{T}_h^{s,n}$ defined in $\Omega_h^{s,n}$ moves on the foreground cutting the underlying elements. Hence, these elements are overlapped (partially or totally) by the structure mesh and they are divided in multiple sub-portions that are, in general, polyhedra. Such elements are named *fluid cut elements*. Therefore, we can define the *cut-mesh* as the polyhedral fluid mesh $\mathcal{T}_h^{f,n}$ that covers the fluid domain $\Omega_h^{f,n}$, composed by the union of all fluid elements in $\mathcal{T}_h$ that are not cut by the structure mesh and all the non-overlapped parts of the cut elements. In our case, referring to Figure 3, we have $\mathcal{T}_h^{s,n} = \mathcal{T}_{h,1}^{s,n} \cup \mathcal{T}_{h,2}^{s,n}$, where $\mathcal{T}_{h,i}^{s,n}$, $i = 1, 2$, represent the meshes corresponding to $\Omega_{h,i}^{s,n}$, $i = 1, 2$, that is the membrane assembly ($i = 1$) and the magnet ring ($i = 2$).

Notice that the cut-mesh has to be updated at each time instant, computing the new intersections generated by the motion of the structure mesh. In order to reduce the complexity of the computation of the mesh intersections, we first need to detect which fluid elements are more likely to intersect the overlapping structure elements, so that the intersection points can be calculated over a reduced set of entities, using a similar approach as in [78]. In this regards, we specifically employed the *Alternating Digital Tree* (ADT) algorithm [79], that is a spatial tree-based search algorithm, which is built upon a hierarchical organization of the mesh elements according to their spatial location. Therefore, this approach is particularly suitable for our problem, where the search can be confined to specific sub-regions of the fluid mesh. Once the intersection points have been computed, we used them to build an interface-fitted sub-tetrahedralization in the cut-elements, that allows for integrating the solution using the standard quadrature rule on each sub-tetrahedron and guarantee numerical accuracy and consistency. In case of more complex interface detection problems, it is possible to consider alternative approaches to ADT for 3D geometric mesh search, such as the *No binary* search [80] or the *dynamic cell-based* search algorithm [81].

If the cut elements are separated by the structure in multiple disjoint fluid sub-elements, they are called *split elements* (see Figure 4). We name $\mathcal{T}_h^X \subseteq \mathcal{T}_h$ the union of the split elements in the background mesh. In XFEM, the classical Finite Elements Lagrangian basis functions defined on the split element are used to build the numerical solution in all the sub-elements, thus requiring the

Prepared using cnmauth.cls
DOI: 10.1002/cnm

duplication of the original d.o.f. for each sub-elements (see Figure 4, right). This allows to have an accurate description of the fluid solution across the structure mesh, possibly characterized by discontinuities [67].

For more details on the computational implementation of XFEM in our scenario, we refer the reader to [73].

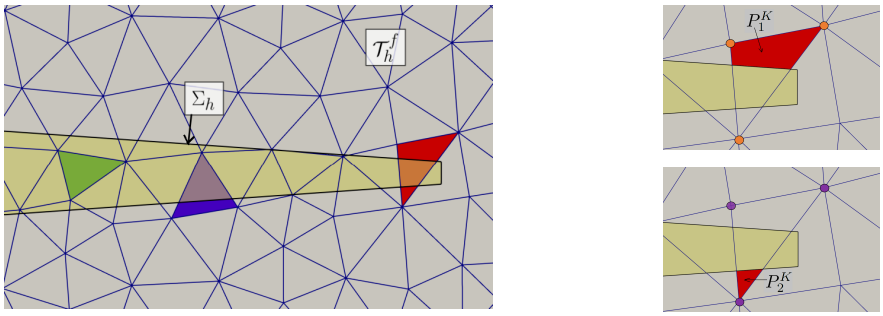

Figure 4. Left: Different fluid elements in XFEM: completely overlapped element (green), partially overlapped cut element (blue) and split element (red). Right: D.o.f. duplication in a split element $K \in \mathcal{T}_h^X$. The same basis functions are used for P_1^K and P_2^K.

Remark 1

We point out that our XFEM strategy is sligthly different to the one originally presented in [70, 71, 82], where the discontinuity was a curve (surface) embedded in a 2D (3D) domain and it was represented as a level-set function. In our framework, from the fluid point of view, the structure domain acts as the "discontinuity" and it is represented with a mesh instead of a level-set function. Despite of this, a numerical approximation $u_h(\mathbf{x})$ on a split element with two fluid sub-elements can be thought as the sum of two contributions: the standard Finite Element part (i.e., the standard basis functions $\varphi_i(\mathbf{x})$ and d.o.f. u_i) and the enrichment term, consisting in the enriched (i.e., doubled) d.o.f. e_i and in the standard basis functions $\varphi_i(\mathbf{x})$ multiplied by the enrichment function $\Phi_i(\mathbf{x})$, namely

$$u_h(\mathbf{x}) = \sum_{i \in I^{std}} u_i \varphi_i(\mathbf{x}) + \sum_{i \in I^{enr}} e_i \varphi_i(\mathbf{x}) \Phi_i(\mathbf{x}),$$

where I^{std} and I^{enr} are the sets of standard and enriched d.o.f., respectively, and $\Phi_i(\mathbf{x})$ is the sign function restricted on the two fluid sub-elements. Notice that, this approximation can be generalized to the case of split elements with three or more fluid sub-elements.

Remark 2

The sub-tetrahedralization of the cut-elements, that in our implementation is delegated to external libraries, such as Triangle [83] for 2D meshing and TetGen [84] for 3D meshing, may become particularly involved in case of complex or irregular geometries. In these cases, there exist alternative approaches for the numerical integration in the cut-elements, that do not require sub-domain partition. For instance, the *enriched interface method* [85] relies on a larger set of integration points and the application of a high order Guassian quadrature rule. However, this technique is based

Prepared using cnmauth.cls
DOI: 10.1002/cnm

on the assumption that the thickness of the structure can be neglected compared with the size of the fluid domain. In our case, the membrane thickness is not negligible and varies along the radial direction; therefore, the approach above should be extended to take into account the overlapped portions of the split elements.

3.2.2. Full discretization As mentioned, for the spatial discretization we considered a DG method in the XFEM framework to manage the numerical solution at the fluid-structure interface Σ_h.

Regarding the fluid problem, we considered standard strong continuity in the fluid domain, except in the proximity of the fluid-structure interface, where we needed to consider again a DG approach to ensure continuity of velocity and tractions between two adjacent fluid mesh elements. Indeed, the presence of the split elements, i.e. general polyhedra, does not allow to easily impose strong continuity. Therefore, we can require only weak continuity in $\mathcal{T}_h^X$, i.e. the union of the split elements in the background mesh; instead, we can have strong continuity on the remaining portion of the fluid domain $\Omega_h^{f,c} = \Omega_h^f \setminus \mathcal{T}_h^X$.

For the structure problem instead, the mesh is always composed of the original tetrahedra, thus standard Finite Elements are considered for its approximation.

According to the previous discussion, we introduce the following discrete spaces in the fluid and structure domains:

$$
\begin{aligned}
X_h^{f,n} &= \left\{ v_h \in L^2(\Omega_h^{f,n}) : v_h \in C^0(\Omega_h^{f,c,n}), v_h|_K \in \mathbb{P}_1(K),\, \forall K \in \mathcal{T}_h^{X,n} \right\}, \\
X_{h,i}^s &= \left\{ \widehat{v}_h \in C^0(\widehat{\Omega}_{h,i}^s) :\, \widehat{v}_h|_K \in \mathbb{P}_1(K),\, \forall K \in \widehat{\mathcal{T}}_{h,i}^s \right\} \quad \text{for } i = 1, 2, \\
X_h^s &= X_{h,1}^s \oplus X_{h,2}^s,
\end{aligned}
$$

and the corresponding spaces for the approximation of fluid velocity and pressure and of structure displacement:

$$
\begin{aligned}
\mathbf{V}_{h,\boldsymbol{\varphi}}^n &= \left\{ \mathbf{v}_h \in [X_h^{f,n}]^3 : \mathbf{v}_h = \mathbf{0} \text{ on } \Gamma_h^{w,n},\, \mathbf{v}_h = \boldsymbol{\varphi} \text{ on } \Gamma_h^{D,n} \right\}, \\
Q_h^n &= X_h^{f,n}, \\
\mathbf{W}_{h,\boldsymbol{\varphi}} &= \left\{ \widehat{\mathbf{w}}_h \in [X_h^s]^3 :\, \widehat{\mathbf{w}}_h = \widehat{\boldsymbol{\varphi}} \text{ on } \widehat{\Gamma}_h^D \right\}.
\end{aligned}
$$

In view of the DG formulation for the fluid problem, we introduce the mean operator $\{\cdot\}$ and the jump operator $[\![\cdot]\!]$, defined over an element face F as:

$$
\{q\} = \frac{1}{2}\left(q_+ + q_-\right) \qquad [\![q]\!] = q_+ - q_-,
$$

where q is a function that assumes values q_+ and q_- on the two sides of face F.

To manage the geometric non-linearity, we considered an explicit treatment of the geometric coupling by taking the first order extrapolation from the previous timestep, i.e. $\Omega_h^{f,n+1} \simeq \Omega_h^{f,n} = \Omega_h^f(\mathbf{d}_h^n)$. To simplify the notation, we omit in what follows the current temporal index $^{n+1}$ for

Prepared using cnmauth.cls
DOI: 10.1002/cnm

variables and domains. We considered the Backward Differentiation Formula of order 1 for the discretization of both the fluid and solid time derivatives and we used a semi-implicit approach for the treatment of the fluid convective term. Let $(\cdot,\cdot)_\Theta$ be the internal product in L^2 in a domain Θ.

Then, we define the following forms:

i) The fluid form

$$\begin{aligned}\mathcal{A}_h^f(\mathbf{u}_h,\mathbf{u}_h^*,p_h;\mathbf{v}_h,q_h) =& \frac{\rho^f}{\Delta t}\,(\mathbf{u}_h,\mathbf{v}_h)_{\Omega_h^{f,n}} + \rho^f\,(\mathbf{u}_h^*\cdot\nabla\mathbf{u}_h,\mathbf{v}_h)_{\Omega_h^{f,n}}\\ &+ 2\mu^f\,(\mathbf{D}(\mathbf{u}_h),\mathbf{D}(\mathbf{v}_h))_{\Omega_h^{f,n}} - (p_h,\nabla\cdot\mathbf{v}_h)_{\Omega_h^{f,n}}\\ &+ (q_h,\nabla\cdot\mathbf{u}_h)_{\Omega_h^{f,n}} + \mathbf{c}_h(\mathbf{u}_h^*,\mathbf{u}_h;\mathbf{v}_h)\\ &+ \mathbf{s}_h(\mathbf{u}_h,p_h;\mathbf{v}_h,q_h) + \mathbf{g}_h(\mathbf{u}_h;\mathbf{v}_h),\end{aligned}$$

which collects the terms of the weak formulation of the stabilized Navier-Stokes equations with convective velocity $\mathbf{u}_h^* = \mathbf{u}_h^n$.

In the previous form, we have considered the correction term of the convective term defined as

$$\begin{aligned}\mathbf{c}_h(\mathbf{u}_h^*,\mathbf{u}_h;\mathbf{v}_h) = \frac{\rho^f}{2}\left((\nabla\cdot\mathbf{u}_h^*)\,\mathbf{u}_h,\mathbf{v}_h\right)_{\Omega_h^{f,n}} &- \sum_{F\in\mathcal{F}_h^{p,n}}\rho^f\,(\{\mathbf{u}_h^*\}\cdot\mathbf{n}[\![\mathbf{u}_h]\!],\{\mathbf{v}_h\})_F\\ &- \sum_{F\in\mathcal{F}_h^{p,n}}\frac{\rho^f}{2}\,([\![\mathbf{u}_h^*]\!]\cdot\mathbf{n}\,\{\mathbf{u}_h\cdot\mathbf{v}_h\})_F\,,\end{aligned}$$

where $\mathcal{F}_h^{p,n}$ is the set of the faces of the split elements in $\mathcal{T}_h^{X,n}$, excluding the portions overlapped by the structure mesh, see [86, 87].

The stabilization term $\mathbf{s}_h(\mathbf{u}_h,p_h;\mathbf{v}_h,q_h)$ corresponds to the *Continuous Interior Penalty* (CIP) stabilization [88], introduced to handle spurious instabilities due to equal order of Finite Elements for velocity and pressure, and have better control on the convective term and on the incompressibility condition. It is defined over the set $\mathcal{F}_h^n$ of the faces of the split elements in $\mathcal{T}_h^{X,n}$ (inluding the overlapped sub-portions) as

$$\begin{aligned}\mathbf{s}_h(\mathbf{u}_h,p_h;\mathbf{v}_h,q_h) =& \gamma_{v1}\sum_{F\in\mathcal{F}_h^n}\xi\,(Re_F)\,h_F^2\,||\mathbf{u}_h^*\cdot\mathbf{n}||_{\infty,F}\,([\![\nabla\mathbf{u}_h\cdot\mathbf{n}]\!],[\![\nabla\mathbf{v}_h\cdot\mathbf{n}]\!])_F\\ &+ \gamma_{v2}\sum_{F\in\mathcal{F}_h^n}\xi\,(Re_F)\,h_F^2||\mathbf{u}_h^*||_{\infty,F}\,([\![\nabla\cdot\mathbf{u}_h]\!],[\![\nabla\cdot\mathbf{v}_h]\!])_F\\ &+ \gamma_p\sum_{F\in\mathcal{F}_h^n}\xi\,(Re_F)\,\frac{h_F^2}{||\mathbf{u}_h^*||_{\infty,F}}\,([\![\nabla p_h]\!],[\![\nabla q_h]\!])_F\,,\end{aligned}$$

where γ_{v1}, γ_{v2} and γ_p are positive penalty parameters, Re_F is the local Reynolds number over the face F, h_F is a characteristic mesh size for F, and $\xi(x) = \min(1,x)$.

Prepared using cnmauth.cls
DOI: 10.1002/cnm

The ghost-penalty stabilization $\mathbf{g}_h(\mathbf{u}_h;\mathbf{v}_h)$ [89] is added to prevent possible instabilities caused by the arbitrarily small dimension of the generated cut elements. It is defined over the set of faces $\mathcal{F}_h^{\Sigma,n}$ crossed by the interface Σ_h^n as

$$\mathbf{g}_h(\mathbf{u}_h;\mathbf{v}_h) = \gamma_g \sum_{F\in\mathcal{F}_h^{\Sigma,n}} \mu^f h_F \left(\llbracket\nabla\mathbf{u}_h\rrbracket\mathbf{n}^F, \llbracket\nabla\mathbf{v}_h\rrbracket\mathbf{n}^F\right)_F,$$

with $\gamma_g > 0$;

ii) The form related to the DG fluid terms over the faces in $\mathcal{F}_h^p$, defined as

$$\begin{aligned}\mathcal{D}_h^f(\mathbf{u}_h,p_h;\mathbf{v}_h,q_h) = &- \sum_{F\in\mathcal{F}_h^{p,n}} \left(\left\{\mathbf{T}^f(\mathbf{u}_h,p_h)\right\}\mathbf{n}^f, \llbracket\mathbf{v}_h\rrbracket\right)_F \\ &- \sum_{F\in\mathcal{F}_h^{p,n}} \left(\llbracket\mathbf{u}_h\rrbracket, \left\{\mathbf{T}^f(\mathbf{v}_h,-q_h)\right\}\mathbf{n}^f\right)_F \\ &+ \sum_{F\in\mathcal{F}_h^{p,n}} \frac{\gamma_{dg}\mu^f}{h_F} \left(\llbracket\mathbf{u}_h\rrbracket, \llbracket\mathbf{v}_h\rrbracket\right)_F,\end{aligned}$$

where $\gamma_{dg} > 0$ is the stability parameter [90];

iii) The structure bilinear form

$$\begin{aligned}\mathcal{A}_h^s\left(\widehat{\mathbf{d}}_h;\widehat{\mathbf{w}}_h\right) = &\frac{1}{\Delta t^2}\left(\widetilde{\rho}^s\widehat{\mathbf{d}}_h, \widehat{\mathbf{w}}_h\right)_{\widehat{\Omega}_h^s} + \left(\widetilde{\lambda}^s\,\nabla\cdot\widehat{\mathbf{d}}_h, \nabla\cdot\widehat{\mathbf{w}}_h\right)_{\widehat{\Omega}_h^s} \\ &+ 2\left(\widetilde{\mu}^s\,\mathbf{D}(\widehat{\mathbf{d}}_h), \mathbf{D}(\widehat{\mathbf{w}}_h)\right)_{\widehat{\Omega}_h^s};\end{aligned}$$

iv) The form $\mathcal{I}_h(\mathbf{u}_h,p_h,\mathbf{d}_h;\mathbf{v}_h,q_h,\mathbf{w}_h)$ corresponding to the DG FSI coupling terms at the fluid-structure interface Σ_h^n [65, 73]:

$$\begin{aligned}\mathcal{I}_h(\mathbf{u}_h,p_h,\mathbf{d}_h;\mathbf{v}_h,q_h,\mathbf{w}_h) = &- \left(\mathbf{T}^f(\mathbf{u}_h,p_h)\mathbf{n}^f, \mathbf{v}_h-\mathbf{w}_h\right)_{\Sigma_h^n} \\ &- \left(\mathbf{T}^f(\mathbf{v}_h,q_h)\mathbf{n}^f, \mathbf{u}_h-\frac{\mathbf{d}_h}{\Delta t}\right)_{\Sigma_h^n} \\ &+ \frac{\gamma_\Sigma\mu^f}{h}\left(\mathbf{u}_h-\frac{\mathbf{d}_h}{\Delta t}, \mathbf{v}_h-\mathbf{w}_h\right)_{\Sigma_h^n},\end{aligned}$$

where $\gamma_\Sigma > 0$ is the penalty parameter associated with the interface Σ;

Prepared using cnmauth.cls
DOI: 10.1002/cnm

v) The functional related to the right hand side formed by the terms arising from time integration and Neumann boundary conditions:

$$\begin{aligned}\mathcal{F}_h(\mathbf{v}_h, q_h, \mathbf{w}_h) = &\frac{\rho^f}{\Delta t}\,(\mathbf{u}_h^n, \mathbf{v}_h)_{\Omega_h^{f,n}} + \sum_{F\in\Gamma^{in}} \left(\Delta P\,\mathbf{n}^f, \mathbf{v}_h\right)_F \\ &+ \frac{1}{\Delta t^2}\left(\widetilde{\rho}^s\left(2\widehat{\mathbf{d}}_h^n - \widehat{\mathbf{d}}_h^{n-1}\right), \widehat{\mathbf{w}}_h\right)_{\widehat{\Omega}_h^s} \\ &+ \left(\mathbf{T}^f(\mathbf{v}_h, q_h)\mathbf{n}^f, \frac{\mathbf{d}_h^n}{\Delta t}\right)_{\Sigma_h^n} - \frac{\gamma_\Sigma \mu^f}{h}\left(\frac{\mathbf{d}_h^n}{\Delta t}, \mathbf{v}_h - \mathbf{w}_h\right)_{\Sigma_h^n}.\end{aligned}$$

The full discretization of problem (2)-(3) reads then as follows: for $n = 0, 1, \ldots$, find $(\mathbf{u}_h, p_h, \mathbf{d}_h) \in \mathbf{V}_{h,\dot{\varphi}} \times Q_h \times \mathbf{W}_{h,\varphi}$ such that $\mathbf{u}_h^0 = \mathbf{0}$, $\mathbf{d}_h^0 = \mathbf{0}$, $\mathbf{d}_h^{-1} = \mathbf{0}$ and

$$\begin{aligned}\mathcal{A}_h^f(\mathbf{u}_h, \mathbf{u}_h^n, p_h; \mathbf{v}_h, q_h) + \mathcal{A}_h^s\left(\widehat{\mathbf{d}}_h; \widehat{\mathbf{w}}_h\right) + \mathcal{D}_h^f(\mathbf{u}_h, p_h; \mathbf{v}_h, q_h) \\ + \mathcal{I}_h(\mathbf{u}_h, p_h, \mathbf{d}_h; \mathbf{v}_h, q_h, \mathbf{w}_h) = \mathcal{F}_h(\mathbf{v}_h, q_h, \mathbf{w}_h) \quad (4)\end{aligned}$$

$\forall\,(\mathbf{v}_h, q_h, \mathbf{w}_h) \in \mathbf{V}_{h,0} \times Q_h \times \mathbf{W}_{h,0}$.

3.3. Numerical settings and parameters

We studied the pump system at fixed pump operating conditions. Therefore, we applied a constant pressure difference ΔP between outlet Γ^{out} and inlet Γ^{in} and an oscillatory motion to the membrane frame (Γ_1^D) and the magnet ring (Γ_2^D).

Boundary conditions (3a)-(3b) define the pressure difference $\Delta P = P^{out} - P^{in} > 0$ acting over the pump, indicating the hydraulic resistance that the wave membrane has to overcome in order to generate positive blood flow in the outlet direction against negative pressure gradients. We fixed the outlet pressure to the standard value for systolic aortic pressure, i.e. $P^{out} = 120$ mmHg. Then, we studied the pump dynamics for different values of pressure parameter ΔP.

Moreover, we modeled the motion imposed on the magnet ring and on the membrane frame by the electromagnetic actuator by means of the Dirichlet condition (3d). Although in the real pump system the control on the oscillations may not be optimal due to instabilities in the electro-mechanical dynamics or manufacturing tolerances, its motion can be approximated with a sinusoid in time in the vertical direction. Therefore, in our simulation the displacement function $\boldsymbol{\varphi}$ has been defined as

$$\boldsymbol{\varphi}(t) = \frac{\Phi}{2}\,\sin(2\pi f t)\,\mathbf{e}_z \qquad t \in (0, T), \quad (5)$$

where f is the excitation frequency of the structure and Φ is the so-called *stroke* parameter. Thus, the pair (f, Φ) defines the *operating point* of the wave membrane. In all our simulations, we have set $f = 120$ Hz, and $\Phi = 1.06$ mm, which are values of interest for real applications of the pump device [91].

DOI: 10.1002/cnm

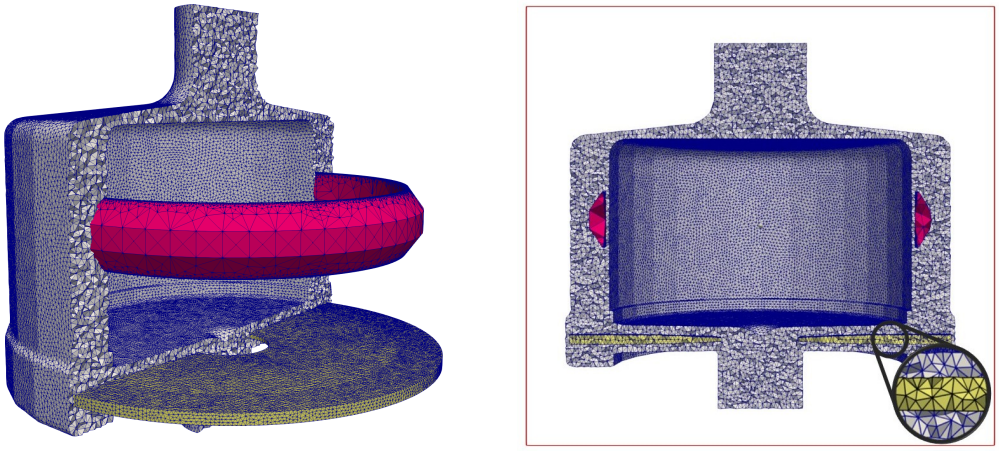

Figure 5. Prospective visualization and section of the fluid mesh $\mathcal{T}_h^f$ (gray), the membrane $\mathcal{T}_h^{s,1}$ (yellow) and magnet mesh $\mathcal{T}_h^{s,2}$ (red).

The unfitted fluid and solid meshes used for the simulations have been shown in Figure 5. The background mesh $\mathcal{T}_h$ has $1.2M$ elements, while the membrane mesh $\mathcal{T}_{h,1}^s$ and the magnet ring mesh $\mathcal{T}_{h,2}^s$ have $280k$ and $50k$ elements, respectively. The size of the fluid and the membrane meshes have been set on the basis of a convergence study, that for sake of simplicity has been carried out in a restricted geometry limited to the pump head region (i.e. part below the magnet ring). Specifically, we checked the that blood flow rate and membrane displacement have reached convergence, in the sense that no significant changes have been observed by further refining the mesh. Notice that, we have removed from the membrane computational domain the step before the membrane frame (i.e., we take $s = 0$ with respect to Figure 2, right) in order to obtain a smooth membrane surface. In addition, we observe that there is a very small gap between the magnet mesh and the side wall of the actuator (Figure 5, right panel); in such region, the use of the unfitted XFEM allowed us to avoid high distortion of the interstitial fluid elements during the vertical oscillation of the magnet.

Concerning the temporal discretization of the simulation interval $(0, T)$, we need to choose a timestep that is sufficiently small to capture the effect of membrane wave propagation on the flow dynamics. Therefore, given the high frequency of membrane vibration, we took $\Delta t = 0.2$ ms, corresponding to less than $1/40$ of the period of oscillation, which is $\tau = 8.33$ ms. The values of the physical parameters of the pump system have been reported in Table I. We remind that the Lamé's parameters used in Section 3 can be derived as $\lambda_i^s = E_i^s \nu_i^s / (1+\nu_i^s)(1-2\nu_i^s)$ and $\mu_i^s = E_i^s / 2(1+\nu_i^s)$, for $i = 1, 2$.

The linear system obtained at each timestep after the XFEM-based discretization has been solved with a monolythic approach with a GMRES solver preconditioned by a block Gauss-Seidel preconditioner. The problem has been solved in the C++ finite element LIFEV library [92] in a multi-thread parallel environment. In particular, we employed 10 cores (Intel processor Xeon E5-4610 v2) with 2.3 GHz frequency and a RAM of 252 GB. The overall simulation time, including calibration of penalty parameters, amounts to approximately 2 weeks.

Prepared using cnmauth.cls
DOI: 10.1002/cnm

Physical parameter	**Value**	**Unit**
ρ^f : Blood mass density	1	$[g/cm^3]$
μ^f : Blood dynamic viscosity	0.035	$[(dyne/cm^2) \cdot s]$
ρ_1^s : Membrane mass density	1.125	$[g/cm^3]$
E_1^s : Membrane Young's modulus	$1.686 \cdot 10^7$	$[dyne/cm^2]$
ν_1^s : Membrane Poisson's ratio	0.49	
ρ_2^s : Magnet mass density	7.85	$[g/cm^3]$
E_2^s : Magnet Young's modulus	$2.05 \cdot 10^{12}$	$[dyne/cm^2]$
ν_2^s : Magnet Poisson's ratio	0.28	

Table I. Values of the physical parameters of the main components of the pump system used in the numerical experiments.

4. NUMERICAL RESULTS

In this section, we report 3D numerical results obtained by solving problem (4) for different working conditions of the pump system, using the numerical settings and the physical parameters detailed in Section 3.3. Specifically, we analyzed the fluid dynamics induced by the membrane wave deformation in Section 4.1 and the blood shear rate in Section 4.2. Then, in Section 4.3, we compared the simulation results for different pressure conditions and finally in Section 4.4 we validated the model against experimental data.

4.1. Flow analysis and membrane deformation

We simulated the pump system in continuous conditions with $T = 25$ ms (that is equivalent to 3 complete oscillations of magnet ring and membrane frame) with pressure gradient $\Delta P = 50$ mmHg. The penalty parameters used for this simulation were: $\gamma_\Sigma = 10^6$, $\gamma_{dg} = 10^3$, $\gamma_{v1} = 5 \cdot 10^{-2}$, $\gamma_{v2} = 5 \cdot 10^{-1}$, $\gamma_p = 5 \cdot 10^{-2}$ and $\gamma_g = 1$.

A view of the simulation results is reported in Figure 6, where the vertical displacement of the flexible membrane, the fluid velocity (left panel) and pressure (right panel) fields are shown in a cross-sectional view of the pump domain at time $t = 18.8$ ms, when the membrane frame reaches its top dead center during the third oscillation. Such results confirm that the propelling action of the wave membrane succeeds in generating positive outflow, despite the adverse pressure difference existing between the endings of the pump domain. In particular, referring to the right panel of Figure 6, we can identify three sub-regions in the pressure field: i) a low-pressure area (region A), extending from the inlet down to the membrane frame; ii) a high-pressure area (region B), in proximity to the outlet channel; and the so-called *fluid pocket* (region C), consisting of the fluid portion enclosed between the wave membrane and the pump head flange. The propagation of the fluid pockets in the pump head is at the core of wave pumping mechanism: indeed, by means of the progressive wave, the membrane actively transports the fluid pocket from region A to region B, going against the pressure gradient. In addition, by looking at the pressure field in the remaining part of the pump domain, outside the pump head region, we can see that the pressure gradient favors blood propulsion through the pump: specifically, in region A, blood flows from the inlet (green)

Prepared using cnmauth.cls
DOI: 10.1002/cnm

down to the membrane frame (blue); while, in region B, it is propelled from the membrane tip (red) to the outlet channel (orange).

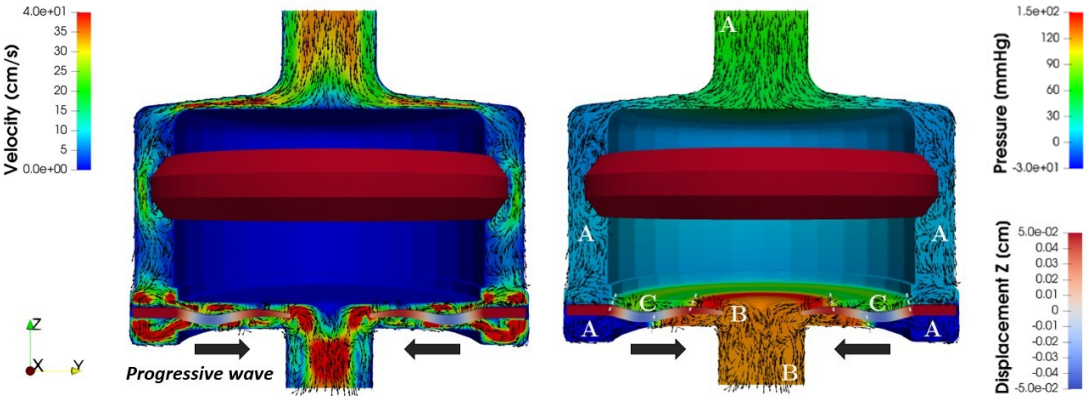

Figure 6. Vertical slice visualization of the three-dimensional flexible membrane vertical displacement, fluid velocity (left) and pressure (right) fields in the full pump domain at time $t = 18.8$ ms.

The success of the wave membrane pumping technology is also confirmed by the analysis of the volume balance reported in Figure 7, left, where we showed the evolution in time of the incoming and outcoming blood volumes V_{in} and V_{out}, representing the volumes of blood entering in and exiting from the pump domain, respectively. These volume quantities were computed integrating the corresponding volumetric flow rate using the trapezoidal rule. Hence, we have $V_\beta^n = \frac{\Delta t}{2}(Q_\beta^n + Q_\beta^{n-1})$, $\beta = \{in, out\}$, where Q_{in} and Q_{out} are the computed pump inflow and outflow rates, respectively. Notice that, after a short interval of adaptation, the two curves V_{in} and V_{out} start oscillating with the same period of the membrane vibrations. Since the values of the divergence of the velocity are very small ($\|\nabla \cdot \mathbf{u}\| < 3 \cdot 10^{-4}\, 1/s$), the small discrepancy between V_{in} and V_{out} is due to the slight incremental variation of the membrane volume $\Delta V_s^n = |\Omega_{h,1}^{s,n}| - |\Omega_{h,1}^{s,n-1}|$, with $\Omega_{h,1}^s$ the discretized membrane domain. Indeed, we have $V_{out}^n - V_{in}^n \simeq \Delta V_s^n$ for all n. Since the magnet ring is a rigid structure, it was not considered in the volume balance. Notice that the observed variation of the membrane volume corresponds to a relative change of less than $2‰$ of the membrane volume. This small variation is explained by the not completely incompressibility of the membrane ($\nu_1^s = 0.49$) and by the numerical approximation. Nevertheless, we verified that such volume variation decreases when the mesh size h is reduced.

We also studied the displacement in time of three key points of the membrane section (see Figure 7, middle): the leading edge (blue), extracted from the membrane frame, the trailing edge (red), in correspondence to the membrane tip, and a third point in-between in the membrane section (green), see Figure 7, right. Since the motion of the membrane frame is governed by (5), the leading edge oscillates between -0.53 mm and 0.53 mm with an excitation frequency equal to 120 Hz. The displacement curves of the midpoint and the trailing edge also become periodic, with the same frequency of the leading edge. In particular, we can notice that the midpoint shows an oscillation amplitude that is smaller than the one of the leading edge, that is likely due to the damping effect

Prepared using cnmauth.cls
DOI: 10.1002/cnm

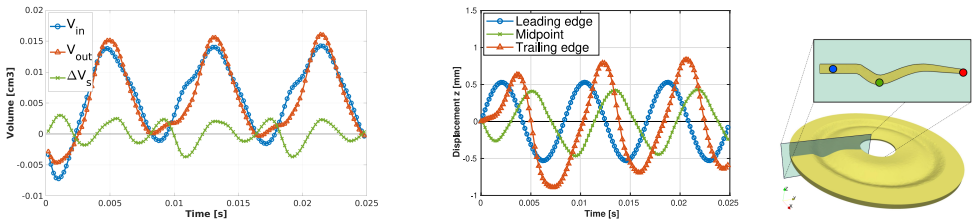

Figure 7. Left: Volume conservation through time. Middle: Vertical displacement of three points of the membrane through time. Right: The three points of the membrane section: the leading edge (blue), the trailing edge (red) and a midpoint in between (green).

of the surrounding viscous fluid on the membrane motion. However, the trailing edge actually is the point that undergoes to the highest displacement, because the most internal portion of the membrane is thinner and therefore it offers less inertial resistance to the wave elastic motion. In fact, the cross-section of the membrane is designed to make the membrane tip reach the quasi-contact configuration with the pump head flanges, allowing for the isolation of the fluid pockets and for the blockage of possible backflows. Nonetheless, the trailing edge never reaches the collision point with the pump flanges in our simulations, in agreement with the theoretical results reported in [75, 76].

Next, we studied more in detail the effect of the wave propagation on the flow dynamics during the whole cycle of membrane oscillation. To this aim, in Figure 8, we analyzed the dynamics in the pump head region for four different time instants in the third period of oscillation of the membrane frame, showing for each time point the radial velocity of the flexible membrane, the blood velocity (left) and pressure (right) fields.

i) In Figure 8a, the membrane frame has returned back to its initial position coming from below. During this upwards vertical displacement, part of the blood coming from the inlet flows above the membrane wave, leading to the formation of an upper fluid pocket (Pocket A), while the remaining part is gathered in the low pressure area below the membrane frame. Meanwhile, in the most internal part of the pump head, another fluid pocket (Pocket B) below the membrane is transported towards the outlet channel thanks to the progressive propagation of the membrane wave. Notice that the simultaneous propagation of two fluid pockets is made possible by the high frequency of oscillation that introduces a second mode of deformation in the elastic membrane. We can also notice some recirculation areas nearby the membrane frame and in proximity to the membrane tip, caused by the flapping motion of the membrane [93].

ii) When the membrane frame reaches the top dead center (time $t = 18.8$ ms), the formation of the upper fluid pocket (Pocket A) is completed and the blood below the membrane frame reaches its point of maximum accumulation (see Figure 8b). While the membrane tip is raising to reduce potential backflows, we can observe a local increase of the pressure in that area that contributes to the blood propulsion towards the outlet. Nonetheless, the ongoing vortex

Prepared using cnmauth.cls
DOI: 10.1002/cnm

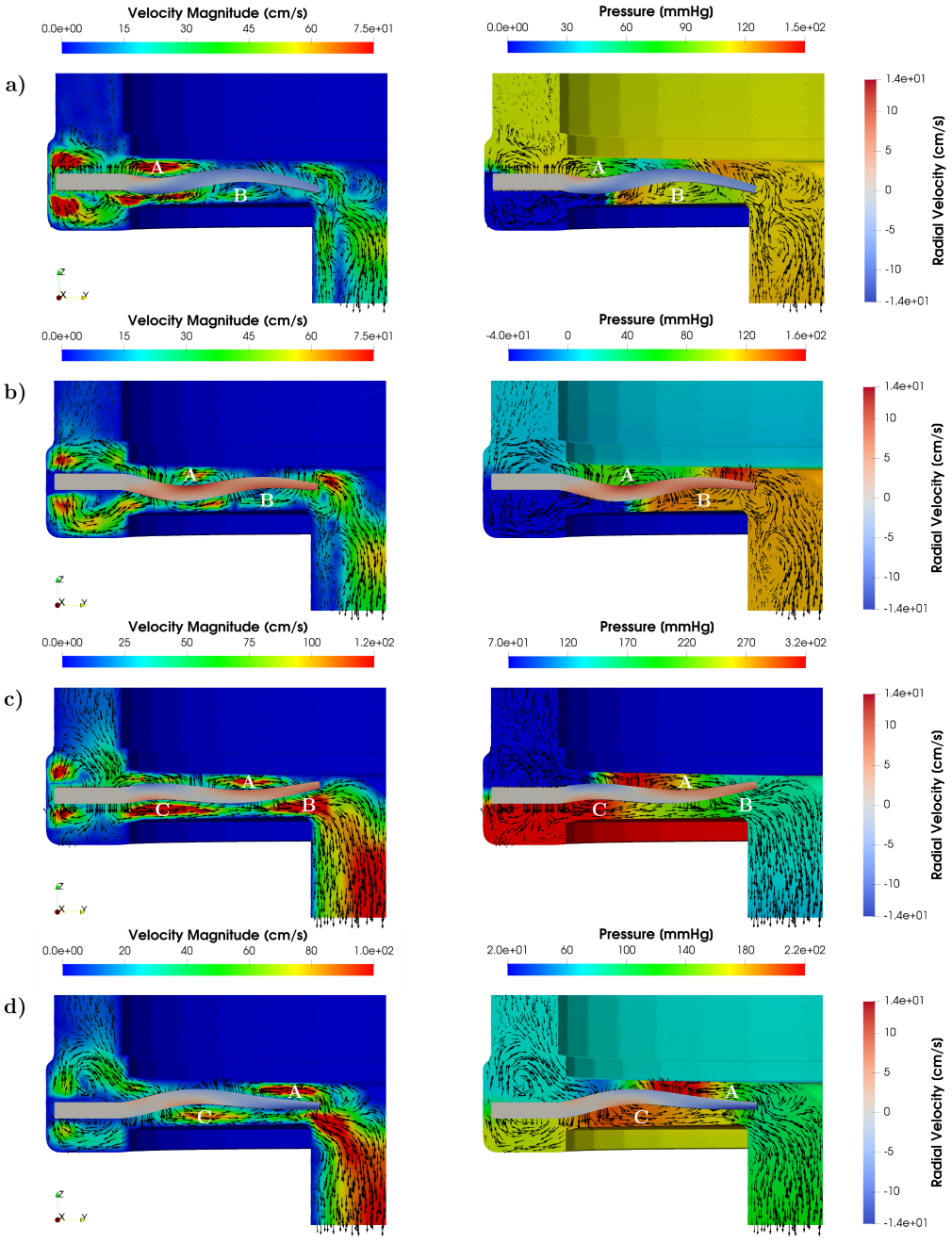

Figure 8. Visualization of the velocity field (left) and of the pressure field (right) in a vertical section of the pump head region for four different time istants: a) $t = 16.6$ ms, b) $t = 18.8$ ms, c) $t = 20.8$ ms, and d) $t = 22.8$ ms. Capital letters A, B and C indicate the fluid pockets, getting formed and transported by wave propagation.

dynamics below the trailing edge of the membrane seems to hamper the full release of the lower fluid pocket (Pocket B) in the outlet channel, penalizing the overall outflow.

iii) As the membrane frame moves downwards (Figure 8c), it compresses the fluid accumulated in the area below during the ascending phase. This causes a drastic increase of the pressure

Prepared using cnmauth.cls
DOI: 10.1002/cnm

below the membrane, that strongly propels the blood in the outlet direction, contributing to the formation of a new lower fluid pocket (Pocket C). Above the flexible membrane, the upper fluid pocket (Pocket A) proceeds in its radial propagation and the tip of the membrane has reached its quasi-contact configuration with the superior pump flange. We can observe that the velocity values around the quasi-contact region are very low, indicating that potential backflows are blocked or minimized. Moreover, the upper quasi-contact configuration allows to achieve the point of maximum delivery of the fluid pocket below (Pocket B). The combination of these phenomena results in successful pumping dynamics and in rapid increase of the blood outflow.

iv) Then, the membrane frame reaches the bottom dead center, completing the formation of the new fluid pocket (Pocket C) below the flexible membrane, see Figure 8d. Furthermore, blood from the upper pocket (Pocket A) is delivered into the outlet channel, and the cycle can restart.

We conclude our analysis of the flow patterns in the blood pump by noticing recirculation regions around the magnet ring (see Figure 6, left) and nearby the outlet section (see Figure 8b, left). In view of a clinical analysis of the pump, the effect of recirculation regions needs to be closely investigated, because it may lead to local thrombus formation, especially if it comes with flow stagnation [94, 95]. However, in this case, the flow in the recirculation areas is continuously disturbed, making the risk of thrombogenesis very low. Nonetheless, we remark that alternative designs of the CorWave LVAD are in development with the aim to reduce the risk of recirculations and improve hemocompatibility.

4.2. Blood shear rate analysis

In this section, we want to provide very preliminary results about the blood shear rate generated by the pump and its implications. This is motivated by the knowledge that high hydrodynamic shear stress conditions in LVADs are strictly linked to blood adverse events, because they may cause blood cells damage and consequent leak of hemoglobin (hemolysis), or trigger von Willebrand factor (VWF) adhesion, leading to platelet aggregation and thrombogenesis [96].

In Figure 9, we report the values of the shear rate in the fluid domain and at the interfaces with the wave membrane and the magnet ring at time $t = 20.8$ ms, when the pump outflow rate is maximum and the magnet ring and the membrane frame return to their initial position with maximum velocity (see Figure 8c). We can observe that the areas with higher shear rate (shear $> 1500\ s^{-1}$) are located in the pump head region (Point 1), where the fluid pockets are transported by the membrane progressive wave with high velocity, and in the upper part of the pump domain (Point 2), where blood flows in a narrow channel. In particular, peak values of shear rate around $3500 - 4500\ s^{-1}$ are reached under the flexible membrane, where the blood velocity is higher than $1\ m/s$, and, in particular, at the periphery of the membrane disc (Point 3). However, the observed shear values are still inferior than $5000\ s^{-1}$, that is the threshold value for the start of VWF-mediated platelet adhesion process [97]. Moreover, since the flow is very disturbed in that area, the exposure time is very short, furtherly reducing the risk of hemolysis or thrombosis. In particular, in the right-bottom

Prepared using cnmauth.cls
DOI: 10.1002/cnm

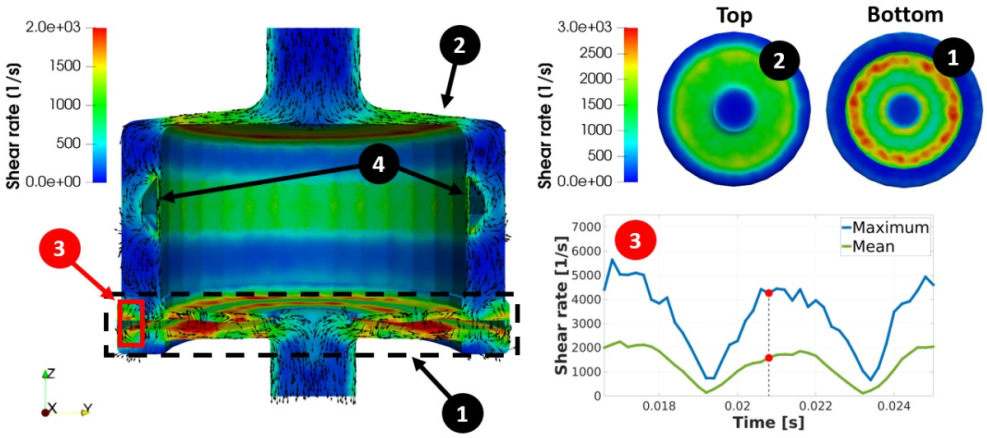

Figure 9. Study of the blood shear rate in the fluid domain. Visualization of the shear rate at time $t = 20.8$ ms on the cross section (left panel) and on the superior and inferior external pump surfaces (right superior panel). The points of interest are: 1) pump head region, 2) superior pump housing surface, 3) side of membrane frame, and 4) magnet ring gap. In particular for Point 3, we show the trend in time of the maximum and the mean values of shear rate in the control volume highlighted by the red box (right inferior panel).

panel of Figure 9, we checked the evolution in time of the shear rate at the side of the membrane frame, by looking at the maximum and the mean values achieved in this area (see red box in Point 3) during the third period of membrane oscillation. The plot highlights that the trend of the shear rate is periodic and that the maximum value in this region, i.e. $5640\ s^{-1}$, is reached during the upward displacement of the membrane frame at time $t = 16.6$ ms (see Figure 8a). Nevertheless, this value is still one order of magnitude smaller than the reference critical value of $42000\ s^{-1}$, that corresponds to the areal strain limit for red blood cells [98].

Another region of interest for shear analysis is the gap between the magnet ring and the pump walls (Point 4). In this area, shear rate is actually smaller than $1000\ s^{-1}$, in accordance with the lower magnitude of fluid velocity, and it decreases to less than $300\ s^{-1}$ when the magnet reaches the top or the bottom dead center (zero velocity). The size of the gap as well as the shape of the magnet ring are currently under study to minimize any hemolitic impact.

4.3. Parametric analysis

In this section we compare the pump performance for different pressure conditions, varying the value of ΔP. In particular we considered $\Delta P \in \{50,\ 55,\ 60\}$ mmHg, being these values taken from the range of standard head pressure conditions used for *in-vitro* and *in-vivo* tests, as in [99, 100]. For this set of simulations, we used $T = 20$ ms. Table II reports the values of the penalty parameters used for this set of simulations to ensure stability for each flow regime.

As the pressure difference ΔP acting over the pump between outlet and inlet increases, the hydraulic resistance inside the pump gets higher and as a consequence, for a fixed operating point of the membrane, the pump outflow gets smaller. This is confirmed by the results reported in the left plot of Figure 10, where we see that the amplitude of the outflow volume rate curves is lower when the pressure difference ΔP is larger. Notice that, although in all the cases there are time intervals

Prepared using cnmauth.cls
DOI: 10.1002/cnm

	$\Delta P = 50$ mmHg	$\Delta P = 55$ mmHg	$\Delta P = 60$ mmHg
γ_Σ	10^6	10^6	10^6
γ_{dg}	10^3	10^3	10^3
γ_g	1	1	1
γ_{v1}	0.05	0.05	0.5
γ_{v2}	0.5	0.5	5
γ_p	0.05	0.1	0.1

Table II. Penalty stability parameters for different pressure conditions.

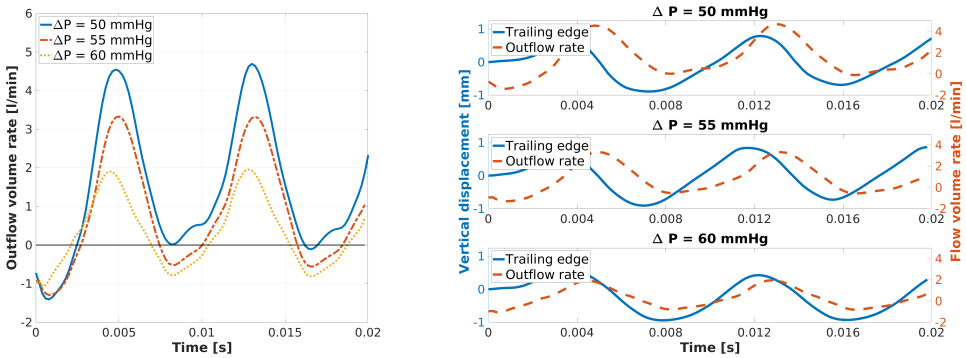

Figure 10. Left: Time profile of the outflow volume rate for three different pressure head conditions ΔP. Right: Vertical displacement of the trailing edge (solid line) for each ΔP value, in relation with the outflow volume rate (dashed line).

with negative outflow, the average in time of the outflow rate is always positive, as required by the correct functioning of the pump.

Furthermore, in the right panel of Figure 10, we displayed in the same figure the pump outflow rate and the vertical displacement of the trailing edge (corresponding to the membrane tip, as in Figure 7, right). Even though the displacement curve is not significantly affected by the different pressure conditions, we can notice that the trailing edge precedes the outflow curve in all the three cases. Indeed, as discussed in Section 4.1, the trailing edge is strictly related to the isolation and the release of the fluid pockets into the outlet channel. Therefore, its displacement drives the time evolution of the outflow volume rate with a small delay due to the time needed for the propagation of the blood from the fluid pocket throughout the outlet channel.

4.4. Validation against experimental measures

As a conclusion, we report results about the validation of the proposed numerical model. To this aim, we compared our simulation results with experimental measurements obtained when testings the blood pump in the same operating conditions. In particular, the hydraulic performance of the blood pump is assessed by means of *in vitro* testings perfomed in a pump characterization bench, consisting of a reservoir and tubing in which the hydraulic resistance can be set by adding centrifugal pumps in a series circuit with the CorWave LVAD. This system is equipped with a polycarbonate hose-barb pressure sensor (PendoTECH), to measure the head pressure arisen between the outlet

Prepared using cnmauth.cls
DOI: 10.1002/cnm

and the inlet of the pump, and with an ultrasonic flowmeter clamped adjacent to the LVAD outlet, to measure the pump outflow volume rate. Therefore, for any given operating point of the wave membrane, we can combine such measurements in pressure-flow data curves, called *HQ curves*, which describe the hydraulic performance of the pump when exposed to different pressure conditions.

Specifically, we have at our disposal the HQ curve of the pump when the operating point of the membrane is fixed to $f = 120$ Hz and $\Phi = 1.06$ mm (Figure 11). Each data point is given by the average in time of the head pressure P^{data} and the corresponding ouflow rate Q^{data}. The slope of the curve is similar to the one of other reference HQ curves of centrifrugal LVADs found in literature (see Figure 3B and 3C in [100]), indicating that, for this operating point, the sensitivity of the pump is in line with the standards in the LVAD community. In Figure 11 we show also the numerical outflow flow rate Q^{sim} corresponding to the pressure differences $\Delta P \in \{50,\ 55,\ 60\}$ mmHg. Here, we observe a very good agreement between numerical results and experimental findings.

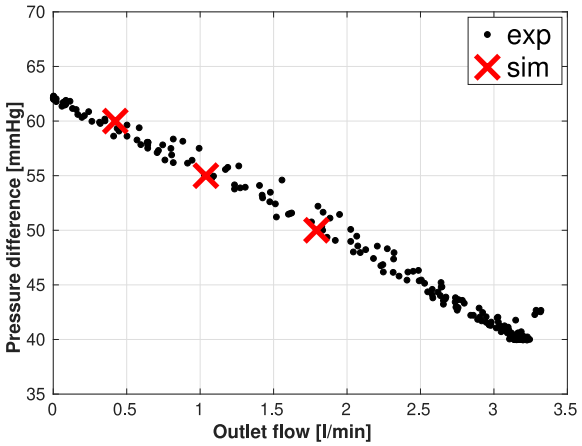

Figure 11. Validation of the model results (red crosses) against the experimental data (black dots).

To quantify the discrepancy, in Table III we reported the comparison between the estimated flow rate Q^{sim} with the experimental data Q^{data}, where the latter corresponds to the measurement associated to the data point that minimizes $|P^{data} - \Delta P|$.

	$\Delta P = 50$ mmHg	$\Delta P = 55$ mmHg	$\Delta P = 60$ mmHg
Q^{data}	$1.834\ \frac{\text{l}}{\text{min}}$	$1.091\ \frac{\text{l}}{\text{min}}$	$0.352\ \frac{\text{l}}{\text{min}}$
Q^{sim}	$1.792\ \frac{\text{l}}{\text{min}}$	$1.039\ \frac{\text{l}}{\text{min}}$	$0.400\ \frac{\text{l}}{\text{min}}$
$\lvert Q^{data} - Q^{sim}\rvert$	$0.042\ \frac{\text{l}}{\text{min}}$	$0.052\ \frac{\text{l}}{\text{min}}$	$0.048\ \frac{\text{l}}{\text{min}}$

Table III. Experimental and simulation data for the model validation against experimental mesures.

These results highlight a very good quantitative agreement with the experimental findings, meaning that the numerical model is able to quantitatively reproduce the pump dynamics with good

Prepared using cnmauth.cls
DOI: 10.1002/cnm

confidentiality for the analyzed pressure conditions. Indeed, the prediction errors are small for all considered ΔP; in particular, the relative error is lower than 5% for $\Delta P = \{50, 55\}$ mmHg, that are the working conditions corresponding to higher pump flow support. However, we note that the operating conditions of the pump considered for the model validation do not correspond with those required for the final application of the pump.

5. CONCLUSIONS

In this work we numerically studied the novel wave membrane technology employed in progressive wave blood pumps, in view of the optimization of the device performance. To this aim, we simulated the fluid-structure interaction between the membrane and the blood flow in a realistic 3D pump domain using the XFEM-DG technique. This unfitted technique allowed us to simply handle the *quasi-contact* configuration between the membrane and the pump walls thanks to a fixed fluid mesh, with no need of remeshing. Then, we discussed the effect of the progressive propagation of the membrane on the blood dynamics, highlighting the mechanisms that allow the pump to propel blood against a negative pressure gradient. We also validated our numerical model against experimental measures at different pressure conditions.

We can conclude that our computational model is able to capture with excellent accuracy the behavior of the pump, despite the simplifications underneath its modeling. This showed, for the first time, that XFEM is a reliable method to handle real-life industrial problems. Therefore, we believe that this work together with future computational studies represent reliable tools for the prediction of the hydraulic performance of the pump under different working conditions and to support the device design.

The design of the pump and of the membrane has recently undergone significant revisions and improvements, in order to increase the hydraulic power and optimize the flow field. We plan, for future studies, to use our numerical model to evaluate and optimize the new pump design, examining the performance across a wider range of clinical conditions, including generation of physiologic pulse hemodynamics, and simulating operating points with higher amplitudes of oscillation of the membrane frame. To achieve this, we are working to further develop the numerical model, in particular to include a contact model to study further the interaction between the oscillating membrane and the pump housing.

ACKNOWLEDGEMENT

This project has received funding from the European Union's Horizon 2020 research and innovation programme under the Marie Skłodowska-Curie grant agreement ROMSOC N. 765374. MM, SZ and CV are members of the INdAM Research group GNCS. SZ has been partially funded by the Italian research project MIUR PRIN17, number 201744KLJL, "Virtual Element Methods: Analysis and Applications". The authors wish to acknowledge Charlotte Rasser, Carl Botterbusch, François Cornat, and Trevor Snyder from CorWave SA for their assistance in manuscript editing and revision.

Prepared using cnmauth.cls
DOI: 10.1002/cnm

References

1. Savarese G, Lund LH. Global public health burden of heart failure. *Cardiac failure review* 2017; **3**(1):7.
2. Vos T, Abajobir AA, Abate KH, Abbafati C, Abbas KM, Abd-Allah F, Abdulkader RS, Abdulle AM, Abebo TA, Abera SF, *et al.*. Global, regional, and national incidence, prevalence, and years lived with disability for 328 diseases and injuries for 195 countries, 1990–2016: a systematic analysis for the global burden of disease study 2016. *The Lancet* 2017; **390**(10100):1211–1259.
3. Alba AC, Delgado DH. The future is here: ventricular assist devices for the failing heart. *Expert Review of Cardiovascular Therapy* 2009; **7**(9):1067–1077, doi:10.1586/erc.09.86.
4. Bartoli C, Dowling R. The next wave of mechanical circulatory support devices. *Cardiac Interventions Today* 2019; **13**(1):53–59.
5. Cohn WE, Timms DL, Frazier OH. Total artificial hearts: past, present, and future. *Nature Reviews Cardiology* 2015; **12**(10):609.
6. Griffith BP, Kormos RL, Borovetz HS, Litwak K, Antaki JF, Poirier VL, Butler KC. HeartMate II left ventricular assist system: from concept to first clinical use. *The Annals of thoracic surgery* 2001; **71**(3):S116–S120.
7. Westaby S, Banning AP, Jarvik R, Frazier OH, Pigott DW, Jin XY, Catarino PA, Saito S, Robson D, Freeland A, *et al.*. First permanent implant of the Jarvik 2000 Heart. *The Lancet* 2000; **356**(9233):900–903.
8. Bourque K, Gernes DB, Loree HM, Richardson JS, Poirier VL, Barletta N, Fleischli A, Foiera G, Gempp TM, Schoeb R, *et al.*. HeartMate III: pump design for a centrifugal LVAD with a magnetically levitated rotor. *ASAIO journal* 2001; **47**(4):401–405.
9. LaRose JA, Tamez D, Ashenuga M, Reyes C. Design concepts and principle of operation of the heartware ventricular assist system. *Asaio Journal* 2010; **56**(4):285–289.
10. Saito S, Yamazaki K, Nishinaka T, Ichihara Y, Ono M, Kyo S, Nishimura T, Nakatani T, Toda K, Sawa Y, *et al.*. Post-approval study of a highly pulsed, low-shear-rate, continuous-flow, left ventricular assist device, evaheart: a japanese multicenter study using j-macs. *The Journal of Heart and Lung Transplantation* 2014; **33**(6):599–608.
11. Meyer AL, Kuehn C, Weidemann J, Malehsa D, Bara C, Fischer S, Haverich A, Strüber M. Thrombus formation in a HeartMate II left ventricular assist device. *The Journal of thoracic and cardiovascular surgery* 2008; **135**(1):203–204.
12. Behbahani M, Behr M, Hormes M, Steinseifer U, Arora D, Coronado O, Pasquali M. A review of computational fluid dynamics analysis of blood pumps. *European Journal of Applied Mathematics* 2009; **20**(4):363–397.
13. Castagna F, Stöhr E, Pinsino A, Cockcroft J, Willey J, Garan A, Topkara V, Colombo P, Yuzefpolskaya M, McDonnell B. The unique blood pressures and pulsatility of lvad patients: current challenges and future opportunities. *Current hypertension reports* 2017; **19**(10):85.
14. Taylor CA, Figueroa CA. Patient-specific modeling of cardiovascular mechanics. *Annual Review of Biomedical Engineering* 2009; **11**:109–134.
15. Smith NP, Nickerson DP, Crampin EJ, Hunter PJ. Multiscale computational modelling of the heart. *Acta Numerica* 2004; **13**:371–431.
16. Colli Franzone P, Pavarino LF, Scacchi S. *Mathematical Cardiac Electrophysiology*. Springer, 2014.
17. Quarteroni A, Dedè L, Manzoni A, Vergara C. *Mathematical Modelling of the Human Cardiovascular System - Data, Numerical Approximation, Clinical Applications*. Cambridge University Press, 2019.
18. Quarteroni A, Rozza G. Optimal control and shape optimization of aorto-coronaric bypass anastomoses. *Mathematical Models and Methods in Applied Sciences* 2003; **13**(12):1801–1823.
19. Lassila T, Manzoni A, Quarteroni A, Rozza G. Boundary control and shape optimization for the robust design of bypass anastomoses under uncertainty. *ESAIM: Mathematical Modelling and Numerical Analysis* 2013; **47**(4):1107–1131.
20. Morganti S, Brambilla N, Petronio AS, Reali A, Bedogni F, Auricchio F. Prediction of patient-specific post-operative outcomes of TAVI procedure: the impact of the positioning strategy on valve performance. *Journal of biomechanics* 2016; **49**(12):2513–2519.
21. Bianchi M, Marom G, Ghosh RP, Rotman OM, Parikh P, Gruberg L, Bluestein D. Patient-specific simulation of transcatheter aortic valve replacement: impact of deployment options on paravalvular leakage. *Biomechanics and modeling in mechanobiology* 2019; **18**(2):435–451.

Prepared using cnmauth.cls
DOI: 10.1002/cnm

22. Sturla F, Ronzoni M, Vitali M, Dimasi A, Vismara R, Preston-Maher G, Burriesci G, Votta E, Redaelli A. Impact of different aortic valve calcification patterns on the outcome of transcatheter aortic valve implantation: a finite element study. *Journal of biomechanics* 2016; **49**(12):2520–2530.
23. Capelli C, Bosi GM, Cerri E, Nordmeyer J, Odenwald T, Bonhoeffer P, Migliavacca F, Taylor AM, Schievano S. Patient-specific simulations of transcatheter aortic valve stent implantation. *Medical & biological engineering & computing* 2012; **50**(2):183–192.
24. Hose DR, Narracott AJ, Griffiths B, Mahmood S, Gunn J, Sweeney D, Lawford PV. A thermal analogy for modelling drug elution from cardiovascular stents. *Computer methods in biomechanics and biomedical engineering* 2004; **7**(5):257–264.
25. Balakrishnan B, Tzafriri AR, Seifert P, Groothuis A, Rogers C, Edelman ER. Strut position, blood flow, and drug deposition: implications for single and overlapping drug-eluting stents. *Circulation* 2005; **111**(22):2958–2965.
26. Vergara C, Zunino P. Multiscale boundary conditions for drug release from cardiovascular stents. *Multiscale Modeling & Simulation* 2008; **7**(2):565–588.
27. Zunino P, D'Angelo C, Petrini L, Vergara C, Capelli C, Migliavacca F. Numerical simulation of drug eluting coronary stents: mechanics, fluid dynamics and drug release. *Computer Methods in Applied Mechanics and Engineering* 2009; **198**(45-46):3633–3644.
28. Ene-Iordache B, Semperboni C, Dubini G, Remuzzi A. Disturbed flow in a patient-specific arteriovenous fistula for hemodialysis: Multidirectional and reciprocating near-wall flow patterns. *J. Biomech.* 2015; **48(10)**:2195–2200.
29. Stella S, Vergara C, Giovannacci L, Quarteroni A, Prouse G. Assessing the disturbed flow and the transition to turbulence in the arteriovenous fistula. *Journal of Biomechanical Engineering* 2019; **141(10)**:101 010.
30. Papantonis D. Numerical prediction of the shear stresses and of the mean stay time for radial flow impellers. *Proceedings of the International Workshop on Rotary blood pumps*, 2nd Univ–Dept. of Surgery, 1991; 63–9.
31. Pinotti M, Rosa ES. Computational prediction of hemolysis in a centrifugal ventricular assist device. *Artificial Organs* 1995; **19**(3):267–273.
32. Wiegmann L, Boës S, De Zélicourt D, Thamsen B, Daners MS, Meboldt M, Kurtcuoglu V. Blood pump design variations and their influence on hydraulic performance and indicators of hemocompatibility. *Annals of biomedical engineering* 2018; **46**(3):417–428.
33. Ghadimi B, Nejat A, Nourbakhsh SA, Naderi N. Shape optimization of a centrifugal blood pump by coupling CFD with metamodel-assisted genetic algorithm. *Journal of Artificial Organs* 2019; **22**(1):29–36.
34. Liu G, Jin D, Zhou J, Zhang Y, Chen H, Sun HS, Hu S, Gui X. Numerical investigation of the influence of blade radial gap flow on axial blood pump performance. *Asaio Journal* 2019; **65**(1):59–69.
35. Wu J, Antaki JF, Wagner WR, Snyder TA, Paden BE, Borovetz HS. Elimination of adverse leakage flow in a miniature pediatric centrifugal blood pump by computational fluid dynamics-based design optimization. *ASAIO journal* 2005; **51 5**:636–43.
36. Wu J, Antaki JF, Bearnson G, Paden D, Maher T, Paden BE. Hydrodynamic and hemodynamic design improvement of the magnetically levitated HEARTQUEST LVAD. *Asaio Journal* 2006; **52**(2):56A.
37. Fraser KH, Taskin ME, Zhang T, Richardson JS, Gellman B, Dasse K, Griffith BP, Wu ZJ. The effect of impeller position on cfd calculations of blood flow in magnetically levitated centrifugal blood pumps. *Summer Bioengineering Conference*, vol. 44038, American Society of Mechanical Engineers, 2010; 119–120.
38. Bonnemain J, Deparis S, Quarteroni A. Connecting ventricular assist devices to the aorta: a numerical model. *Imagine Math*. Springer, 2012; 211–224.
39. Bonnemain J, Malossi ACI, Lesinigo M, Deparis S, Quarteroni A, Von Segesser LK. Numerical simulation of left ventricular assist device implantations: comparing the ascending and the descending aorta cannulations. *Medical engineering & physics* 2013; **35**(10):1465–1475.
40. Prather RO, Ni MW, Divo E, Kassab AJ, DeCampli WM. Pulsatile multiscale fluid-structure interaction modeling for optimal left ventricular assist device implantation. *ASTFE Digital Library*, Begel House Inc., 2018.
41. Sonntag SJ, Zebrowski E, Neidlin M, Hugenroth K, Benkowski R, Motomura T, Kaufmann TAS. Virtual fitting and hemodynamic simulation of the EVAHEART 2 left ventricular assist device and double-cuff tipless inflow cannula. *ASAIO journal (American Society for Artificial Internal Organs: 1992)* 2018; .
42. Pauli L, Nam J, Pasquali M, Behr M. Transient stress-based and strain-based hemolysis estimation in a simplified blood pump. *International journal for numerical methods in biomedical engineering* 2013; **29**(10):1148–1160.

Prepared using cnmauth.cls
DOI: 10.1002/cnm

43. Li H, Gou Z, Huang F, Ruan X, Qian W, Fu X. Evaluation of the hemolysis and fluid dynamics of a ventricular assist device under the pulsatile flow condition. *Journal of Hydrodynamics* 2018; :1–11.
44. Gu K, Guan Z, Chang Y, Gao B, Ling Y, Song Z, Wan F. Hemodynamic effects of pulsatile unloading of left ventricular assist devices (lvad) on intraventricular flow and ventricular stress. *Journal of Biomechanics* 2020; :109 425.
45. Osuna-Orozco R, Chivukula VK, Aliseda A. Numerical modeling of platelet margination and its impact on left ventricular assist device thrombogenicity. *Bulletin of the American Physical Society* 2018; **63**.
46. Molteni A, Masri ZPH, Low KWQ, Yousef HN, Sienz J, Fraser KH. Experimental measurement and numerical modelling of dye washout for investigation of blood residence time in ventricular assist devices. *The International journal of artificial organs* 2018; **41**(4):201–212.
47. Chivukula VK, Beckman JA, Prisco AR, Dardas T, Lin S, Smith JW, Mokadam NA, Aliseda A, Mahr C. Left ventricular assist device inflow cannula angle and thrombosis risk. *Circulation: Heart Failure* 2018; **11**(4):e004 325.
48. Scardulla S, Pasta S, D'Acquisto L, Sciacca S, Agnese V, Vergara C, Quarteroni A, Clemenza F, Bellavia D, M P. Shear stress alterations in the celiac trunk of patients with continuous-flow left ventricular assist device by in-silico and in-vitro flow analysis. *Journal of Heart and Lung Transplantation* 2017; **36(8)**:906–913.
49. Perschall M, Drevet JB, Schenkel T, Oertel H. The progressive wave pump: numerical multiphysics investigation of a novel pump concept with potential to ventricular assist device application. *Artificial organs* 2012; **36**(9).
50. Donea J, Giuliani S, Halleux J. An arbitrary lagrangian-eulerian finite element method for transient dynamic fluid-structure interactions. *Computer methods in applied mechanics and engineering* 1982; **33**(1-3):689–723.
51. Hughes TJR, Liu WK, Zimmermann TK. Lagrangian-Eulerian finite element formulation for incompressible viscous flows. *Computer methods in applied mechanics and engineering* 1981; **29**(3):329–349.
52. Takizawa K, Bazilevs Y, Tezduyar TE, Long CC, Marsden AL, Schjodt K. ST and ALE-VMS methods for patient-specific cardiovascular fluid mechanics modeling. *Mathematical Models and Methods in Applied Sciences* 2014; **24**(12):2437–2486.
53. Hughes TJR, Hulbert GM. Space-time finite element methods for elastodynamics: formulations and error estimates. *Computer methods in applied mechanics and engineering* 1988; **66**(3):339–363.
54. Nguyen H, Reynen J. A space-time least-square finite element scheme for advection-diffusion equations. *Computer Methods in Applied Mechanics and Engineering* 1984; **42**(3):331–342.
55. Tezduyar TE, Sathe S. Modelling of fluid–structure interactions with the space–time finite elements: solution techniques. *International Journal for Numerical Methods in Fluids* 2007; **54**(6-8):855–900.
56. Tezduyar TE, Takizawa K, Moorman C, Wright S, Christopher J. Space–time finite element computation of complex fluid–structure interactions. *International Journal for Numerical Methods in Fluids* 2010; **64**(10-12):1201–1218.
57. Takizawa K, Tezduyar TE, Buscher A, Asada S. Space–time fluid mechanics computation of heart valve models. *Computational Mechanics* 2014; **54**(4):973–986.
58. Peskin C. Flow patterns around heart valves: a digital computer method for solving the equations of motion. *IEEE Transactions on Biomedical Engineering* 1973; (4):316–317.
59. Boffi D, Gastaldi L. The immersed boundary method: a finite element approach. *Computational Fluid and Solid Mechanics 2003*. Elsevier, 2003; 1263–1266.
60. Zhang LT, Gay M. Immersed finite element method for fluid-structure interactions. *Journal of Fluids and Structures* 2007; **23**(6):839–857.
61. Glowinski R, Pan T, Periaux J. A fictitious domain method for dirichlet problem and applications. *Computer Methods in Applied Mechanics and Engineering* 1994; **111**(3-4):283–303.
62. Glowinski R, Pan T, Periaux J. A fictitious domain method for external incompressible viscous flow modeled by navier-stokes equations. *Computer Methods in Applied Mechanics and Engineering* 1994; **112**(1-4):133–148.
63. Bertrand F, Tanguy PA, Thibault F. A three-dimensional fictitious domain method for incompressible fluid flow problems. *International Journal for Numerical Methods in Fluids* 1997; **25**(6):719–736.
64. Gerstenberger A, Wall WA. An extended finite element method/Lagrange multiplier based approach for fluid–structure interaction. *Computer Methods in Applied Mechanics and Engineering* 2008; **197**(19-20):1699–1714.

DOI: 10.1002/cnm

65. Burman E, Fernández MA. An unfitted Nitsche method for incompressible fluid–structure interaction using overlapping meshes. *Computer Methods in Applied Mechanics and Engineering* 2014; **279**:497–514.
66. Massing A, Larson M, Logg A, Rognes M. A Nitsche-based cut finite element method for a fluid-structure interaction problem. *Communications in Applied Mathematics and Computational Science* 2015; **10**(2):97–120.
67. Alauzet F, Fabrèges B, Fernández MA, Landajuela M. Nitsche-XFEM for the coupling of an incompressible fluid with immersed thin-walled structures. *Computer Methods in Applied Mechanics and Engineering* 2016; **301**:300–335.
68. Antonietti PF, Verani M, Vergara C, Zonca S. Numerical solution of fluid-structure interaction problems by means of a high order Discontinuous Galerkin method on polygonal grids. *Finite Elements in Analysis and Design* 2019; **159**:1–14.
69. Moës N, Dolbow J, Belytschko T. A finite element method for crack growth without remeshing. *International Journal for Numerical Methods in Engineering* 1999; **46**:131–150.
70. Belytschko T, Moës N, Usui S, Parimi C. Arbitrary discontinuities in finite elements. *International Journal for Numerical Methods in Engineering* 2001; **50**(4):993–1013.
71. Hansbo A, Hansbo P. An unfitted finite element method, based on nitsche's method, for elliptic interface problems. *Computer methods in applied mechanics and engineering* 2002; **191**(47-48):5537–5552.
72. Gerstenberger A. An XFEM based fixed-grid approach to fluid-structure interaction. PhD Thesis, Technische Universität München 2010.
73. Zonca S, Vergara C, Formaggia L. An unfitted formulation for the interaction of an incompressible fluid with a thick structure via an XFEM/DG approach. *SIAM Journal on Scientific Computing* 2018; **40**(1):B59–B84.
74. Vergara C, Zonca S. *Extended Finite Elements method for fluid-structure interaction with an immersed thick non-linear structure*. 2018; 209–243.
75. Hillairet M, Takahashi T. Collisions in three-dimensional fluid structure interaction problems. *SIAM Journal on Mathematical Analysis* 2009; **40**(6):2451–2477.
76. Cawthorn CJ, Balmforth NJ. Contact in a viscous fluid. Part 1. A falling wedge. *Journal of Fluid Mechanics* 2010; **646**:327–338.
77. Mayer UM, Popp A, Gerstenberger A, Wall WA. 3D fluid–structure-contact interaction based on a combined XFEM FSI and dual mortar contact approach. *Computational Mechanics* 2010; **46**(1):53–67.
78. Massing A, Larson MG, Logg A. Efficient implementation of finite element methods on nonmatching and overlapping meshes in three dimensions. *SIAM Journal on Scientific Computing* 2013; **35**(1):C23–C47.
79. Bonet J, Peraire J. An alternating digital tree (ADT) algorithm for 3D geometric searching and intersection problems. *International Journal for Numerical Methods in Engineering* 1991; **31**(1):1–17.
80. Munjiza A, Andrews KRF. NBS contact detection algorithm for bodies of similar size. *International Journal for Numerical Methods in Engineering* 1998; **43**(1):131–149.
81. Williams JR, Perkins E, Cook B. A contact algorithm for partitioning n arbitrary sized objects. *Engineering Computations* 2004; .
82. Fries T. Overview and comparison of different variants of the XFEM. *PAMM* 2014; **14**(1):27–30.
83. Shewchuk JR. Triangle: Engineering a 2D Quality Mesh Generator and Delaunay Triangulator. *Applied Computational Geometry: Towards Geometric Engineering*, *Lecture Notes in Computer Science*, vol. 1148, Lin MC, Manocha D (eds.). Springer-Verlag, 1996; 203–222. From the First ACM Workshop on Applied Computational Geometry.
84. Si H. TetGen, a delaunay-based quality tetrahedral mesh generator. *ACM Transactions on Mathematical Software (TOMS)* 2015; **41**(2):1–36.
85. Sawada T, Tezuka A. Llm and x-fem based interface modeling of fluid–thin structure interactions on a non-interface-fitted mesh. *Computational Mechanics* 2011; **48**(3):319–332.
86. Temam R. *Navier-Stokes equations: Theory and numerical analysis*, vol. 2. 1977.
87. Di Pietro DA, Ern A. *Mathematical aspects of discontinuous Galerkin methods*, vol. 69. Springer Science & Business Media, 2011.
88. Burman E, Fernández MA, Hansbo P. Continuous interior penalty finite element method for Oseen's equations. *SIAM journal on numerical analysis* 2006; **44**(3):1248–1274.
89. Burman E. Ghost penalty. *Comptes Rendus Mathematique* 2010; **348**(21-22):1217–1220.

DOI: 10.1002/cnm

90. Arnold DN, Brezzi F, Cockburn B, Marini LD. Unified analysis of discontinuous Galerkin methods for elliptic problems. *SIAM journal on numerical analysis* 2002; **39**(5):1749–1779.
91. Botterbusch CN, Lucquin S, Monticone P, Drevet JB, Guignabert A, Meneroud P. Implantable pump system having an undulating membrane 2018. US Patent 9,968,720.
92. Bertagna L, , Deparis S, Formaggia L, Forti D, Veneziani A. The LifeV library: engineering mathematics beyond the proof of concept. *arXiv preprint arXiv:1710.06596* 2017; .
93. Tronchin T. Experimental and numerical characterization of vortex mechanisms of lift generation on a wing in flapping motion 06 2013; .
94. Chiu W, Slepian MJ, Bluestein D. Thrombus formation patterns in the heartmate ii vad-clinical observations can be predicted by numerical simulations. *ASAIO journal (American Society for Artificial Internal Organs: 1992)* 2014; **60**(2):237.
95. Fraser KH, Zhang T, Taskin ME, Griffith BP, Wu ZJ. Computational fluid dynamics analysis of thrombosis potential in left ventricular assist device drainage cannulae. *ASAIO journal (American Society for Artificial Internal Organs: 1992)* 2010; **56**(3):157.
96. Selmi M, Chiu W, Chivukula V, Melisurgo G, Beckman JA, Mahr C, Aliseda A, Votta E, Redaelli A, Slepian MJ, *et al.*. Blood damage in left ventricular assist devices: Pump thrombosis or system thrombosis? *The International journal of artificial organs* 2019; **42**(3):113–124.
97. Schneider S, Nuschele S, Wixforth A, Gorzelanny C, Alexander-Katz A, Netz R, Schneider MF. Shear-induced unfolding triggers adhesion of von willebrand factor fibers. *Proceedings of the National Academy of Sciences* 2007; **104**(19):7899–7903.
98. Behbahani M, Behr M, Hormes M, Steinseifer U, Arora D, Coronado O, Pasquali M. A review of computational fluid dynamics analysis of blood pumps. *European Journal of Applied Mathematics* 2009; **20**(4):363–397.
99. Wiegmann L, Thamsen B, De Zélicourt D, Granegger M, Boës S, Schmid Daners M, Meboldt M, Kurtcuoglu V. Fluid dynamics in the heartmate 3: influence of the artificial pulse feature and residual cardiac pulsation. *Artificial organs* 2019; **43**(4):363–376.
100. Moazami N, Fukamachi K, Kobayashi M, Smedira NG, Hoercher KJ, Massiello A, Lee S, Horvath DJ, Starling RC. Axial and centrifugal continuous-flow rotary pumps: a translation from pump mechanics to clinical practice. *The Journal of heart and lung transplantation* 2013; **32**(1):1–11.

DOI: 10.1002/cnm